

The WiggleZ Dark Energy Survey: the selection function and $z = 0.6$ galaxy power spectrum

Chris Blake^{1*}, Sarah Brough¹, Matthew Colless², Warrick Couch¹, Scott Croom³, Tamara Davis^{4,5}, Michael J. Drinkwater⁴, Karl Forster⁶, Karl Glazebrook¹, Ben Jelliffe³, Russell J. Jurek⁴, I-hui Li¹, Barry Madore⁷, Chris Martin⁶, Kevin Pimblet⁸, Gregory B. Poole¹, Michael Pracy¹, Rob Sharp², Emily Wisnioski¹, David Woods⁹ and Ted Wyder⁶

¹ Centre for Astrophysics & Supercomputing, Swinburne University of Technology, P.O. Box 218, Hawthorn, VIC 3122, Australia

² Anglo-Australian Observatory, P.O. Box 296, Epping, NSW 2121, Australia

³ School of Physics, University of Sydney, NSW 2006, Australia

⁴ Department of Physics, University of Queensland, Brisbane, QLD 4072, Australia

⁵ Dark Cosmology Centre, Niels Bohr Institute, University of Copenhagen, Juliane Maries Vej 30, DK-2100 Copenhagen, Denmark

⁶ California Institute of Technology, MC 405-47, 1200 East California Boulevard, Pasadena, CA 91125, United States

⁷ Observatories of the Carnegie Institute of Washington, 813 Santa Barbara St., Pasadena, CA 91101, United States

⁸ School of Physics, Monash University, Clayton, VIC 3800, Australia

⁹ Department of Physics & Astronomy, University of British Columbia, 6224 Agricultural Road, Vancouver, B.C., V6T 1Z1, Canada

7 March 2018

ABSTRACT

We report one of the most accurate measurements of the three-dimensional large-scale galaxy power spectrum achieved to date, using 56,159 redshifts of bright emission-line galaxies at effective redshift $z \approx 0.6$ from the WiggleZ Dark Energy Survey at the Anglo-Australian Telescope. We describe in detail how we construct the survey selection function allowing for the varying target completeness and redshift completeness. We measure the total power with an accuracy of approximately 5% in wavenumber bands of $\Delta k = 0.01 h \text{ Mpc}^{-1}$. A model power spectrum including non-linear corrections, combined with a linear galaxy bias factor and a simple model for redshift-space distortions, provides a good fit to our data for scales $k < 0.4 h \text{ Mpc}^{-1}$. The large-scale shape of the power spectrum is consistent with the best-fitting matter and baryon densities determined by observations of the Cosmic Microwave Background radiation. By splitting the power spectrum measurement as a function of tangential and radial wavenumbers we delineate the characteristic imprint of peculiar velocities. We use these to determine the growth rate of structure as a function of redshift in the range $0.4 < z < 0.8$, including a data point at $z = 0.78$ with an accuracy of 20%. Our growth rate measurements are a close match to the self-consistent prediction of the Λ CDM model. The WiggleZ Survey data will allow a wide range of investigations into the cosmological model, cosmic expansion and growth history, topology of cosmic structure, and Gaussianity of the initial conditions. Our calculation of the survey selection function will be released at a future date via our website wigglez.swin.edu.au.

Key words: surveys, large-scale structure of Universe, cosmological parameters

1 INTRODUCTION

The pattern of density fluctuations in the low-redshift Universe results from the physical processes which govern the evolution of matter perturbations after the Big Bang. In the

early Universe, the primordial spectrum of fluctuations created by inflation is processed before recombination in a manner depending on the physical matter density, baryon fraction and massive neutrino fraction (e.g. Bond & Efstathiou 1984; Bardeen et al. 1986; Holtzman 1989; Hu & Sugiyama 1996; Eisenstein & Hu 1998). After recombination, perturbations of all scales are amplified by gravity at an identical

* E-mail: cblake@astro.swin.edu.au

rate whilst linear theory applies. This growth rate depends on the matter and dark energy components which drive the cosmic expansion (e.g. Heath 1977; Hamilton 2001; Linder & Jenkins 2003; Percival 2005). The growth of fluctuations enters a non-linear regime at progressively larger scales at lower redshifts: in today’s Universe, only perturbations with Fourier wavenumbers $k < 0.1 h \text{ Mpc}^{-1}$ evolve linearly to a good approximation (e.g. Smith et al. 2003; Jeong & Komatsu 2006; McDonald 2007).

The clustering pattern of galaxies at different redshifts is related to the underlying density fluctuations and may be used to test this model of structure formation. The shape of the clustering power spectrum – the relative amplitudes of large-scale and small-scale modes – depends on the composition of the early Universe and may be used to extract information about the matter and baryon fractions (e.g. Tegmark et al. 2004a; Cole et al. 2005; Percival et al. 2007b). The amplitude of the clustering power spectrum as a function of redshift, together with the pattern of redshift-space distortions induced by galaxy peculiar velocities, can be used to measure the growth rate of structure (e.g. Hamilton 1992; Hawkins et al. 2003; Guzzo et al. 2008; Percival & White 2009). Higher-order or topological descriptors of the density field, such as the bispectrum or genus, can be applied to test whether the initial conditions are consistent with scale-invariant Gaussian random perturbations generated by inflation (e.g. Gott, Dickinson & Melott 1986; Fry & Scherrer 1994; Sefusatti & Komatsu 2007; James, Lewis & Colless 2007).

The interpretation of the shape and amplitude of the galaxy power spectrum is complicated by several factors. Firstly, the manner in which galaxies trace the density field – the “galaxy bias” – is in general a complex function of scale, dark matter halo mass, galaxy type and redshift (Dekel & Lahav 1999; Tegmark & Bromley 1999; Wild et al. 2005; Conway et al. 2005; Percival et al. 2007a; Smith, Scoccamarro & Sheth 2007; Cresswell & Percival 2009). However, the bias of galaxy fluctuations on sufficiently large scales ($k < 0.1 h \text{ Mpc}^{-1}$ at $z = 0$) appears to be well-described by a simple constant of proportionality whose value depends on galaxy type and luminosity, or more fundamentally dark matter halo mass (Peacock & Dodds 1994; Scherrer & Weinberg 1998; Verde et al. 2002). Secondly, small-scale density perturbations eventually begin to evolve in a non-linear fashion requiring more complex modelling techniques such as higher-order perturbation theory or numerical N -body simulations (Smith et al. 2003; Jeong & Komatsu 2006; McDonald 2007). Thirdly, there is a practical challenge of acquiring galaxy survey data across a “fair sample” of the Universe (Tegmark 1997). For the large-scale linear modes of clustering, which provide the most robust link to underlying theory, this sample must map a volume of the order 1 Gpc^3 using of the order 10^5 galaxies. These demands require multi-year campaigns with ground-based telescopes utilizing hundreds of clear nights (Glazebrook & Blake 2005).

Despite these challenges, a series of galaxy redshift surveys have been undertaken to provide such datasets at redshifts $z < 0.5$. The state-of-the-art projects which have mapped the “local” ($z \approx 0.1$) Universe are the 2-degree Field Galaxy Redshift Survey (2dFGRS; Colless et al. 2001) and the Sloan Digital Sky Survey (SDSS; York et al. 2000). The 2dFGRS obtained redshifts for 2×10^5 galaxies covering

1500 deg^2 in the period between 1997 and 2002. The “main” spectroscopic survey of the SDSS gathered 8×10^5 galaxy redshifts over 8000 deg^2 between the years 2000 and 2005. The SDSS project also included observations of 1×10^5 Luminous Red Galaxies (LRGs) reaching up to a redshift $z = 0.5$ (Eisenstein et al. 2001).

These datasets have provided a rich source of information about the clustering of galaxies. For example, power spectra have been extracted for the 2dFGRS by Percival et al. (2001) and Cole et al. (2005); for the SDSS “main” galaxy sample by Pope et al. (2004), Tegmark et al. (2004a) and Percival et al. (2007a); and for the LRGs by Eisenstein et al. (2005), Huetsi (2006), Tegmark et al. (2006) and Percival et al. (2007b). Analysis of these surveys, in combination with the Cosmic Microwave Background fluctuations, has confirmed that we inhabit a low-density Universe where matter today provides only 25 – 30% of the total energy governing the large-scale dynamics, with the rest located in a mysterious “dark energy” component. In addition the baryonic fraction of the matter is only 15 – 20%, with the remainder composed of non-baryonic, cold particles whose nature is currently unknown (e.g. Percival et al. 2002; Tegmark et al. 2004b; Tegmark et al. 2006; Komatsu et al. 2009). The clustering pattern is also sensitive to the presence of hot dark matter such as massive neutrinos, which comprise a small fraction of the energy budget (Elgaroy et al. 2002; Seljak et al. 2005).

These galaxy surveys also describe how the underlying density fluctuations are modulated by galaxy bias (Verde et al. 2002; Wild et al. 2005; Conway et al. 2005; Percival et al. 2007a; Cresswell & Percival 2009). In this context the comparison of power spectrum measurements from the 2dFGRS and SDSS, which targeted galaxy populations selected in blue and red optical wavebands respectively, is of particular interest. When the differing galaxy types in these surveys are assigned linear bias factors, the resulting model fits to the linear-regime power spectra produce best-fitting matter densities which are inconsistent at the statistical level of 2σ . Careful treatment of scale-dependent and luminosity-dependent galaxy bias can potentially explain this discrepancy (Percival et al. 2007a; Sanchez & Cole 2008).

There are strong motivations for extending these large-scale structure measurements to higher redshifts ($z > 0.5$). Firstly, the growth of structure implies that the linear regime of evolving perturbations extends to smaller scales at higher redshifts, enabling cleaner and more accurate model fits. Secondly, the shape of the survey cone allows access to significantly greater cosmic volumes at higher redshift, enabling more accurate determinations of the large-scale power spectrum amplitude. Thirdly, baryon oscillations in galaxy power spectra at different redshifts may be used as a standard ruler to extract the cosmic distance-redshift relation and infer the properties of dark energy (Blake & Glazebrook 2003; Seo & Eisenstein 2003; Hu & Haiman 2003). Fourthly, measurements of the growth of cosmic structure as a function of redshift increases our ability to discriminate between dark energy models including modifications to Einstein’s theory of gravity (Guzzo et al. 2008; Wang 2008; White, Song & Percival 2009).

Our current tools for probing the matter power spectrum at redshifts $z > 0.5$ are limited. The clustering of high-redshift quasars has been studied by the 2dF Quasar

Survey (Outram et al. 2003) and the SDSS (Ross et al. 2009) but the scarcity of QSOs implies that the large-scale clustering measurements are strongly limited by shot noise. Photometric redshifts from imaging surveys have been used to study the projected clustering pattern in redshift slices (Blake et al. 2007; Padmanabhan et al. 2007). However, this approach loses the information from small-scale radial clustering modes (Blake & Bridle 2005) and in particular prevents the extraction of the patterns of peculiar velocities, which are swamped by photometric redshift errors. Alternatively, fluctuations in the Lyman- α forest absorption spectrum on the sight lines to bright quasars have been used to infer the amplitude of small-scale clustering fluctuations in the high-redshift Universe (Croft et al. 2002; McDonald et al. 2005; McDonald et al. 2006). However, this method is potentially susceptible to systematic modelling errors and is only applicable at redshifts $z > 2.3$ where the Lyman- α absorption lines pass into optical wavebands.

The WiggleZ Dark Energy Survey at the Anglo-Australian Telescope (Drinkwater et al. 2010) will provide the next step forwards in large-scale spectroscopic galaxy redshift surveys, mapping a cosmic volume of the order 1 Gpc^3 over the redshift range $z < 1$. The survey, which began in August 2006 and is scheduled to finish in July 2010, is obtaining of the order 200,000 redshifts for UV-selected emission-line galaxies covering of the order 1000 deg^2 of equatorial sky. The principal scientific goal is to measure baryon oscillations in the galaxy power spectrum in redshift bins up to $z = 1$ and provide a robust measurement of the dark energy model. The dataset will also trace the density field over unprecedented cosmic volumes at $z > 0.5$, providing a sample comparable to the SDSS LRG catalogue at $z < 0.5$. Moreover, the spatial overlap between the WiggleZ and LRG catalogues in the redshift range $0.3 < z < 0.5$ will allow careful studies of the systematic effects of galaxy bias on power spectrum estimation.

This paper presents a determination of the current WiggleZ survey selection function and galaxy power spectrum, using a dataset comprising of the order 25% of the final survey observations. The selection function, which describes the angular and radial survey coverage in the absence of clustering, is complicated by the relatively high level of incompleteness in the survey affecting both the parent target catalogues and the spectroscopic follow-up observations (although this latter type of incompleteness will decrease as the survey progresses). However, we demonstrate that despite these complications the galaxy clustering power spectrum may be successfully extracted and already provides accurate tests of the cosmological model that rival lower-redshift surveys.

The structure of this paper is as follows: in Section 2 we present a detailed account of the survey selection function including the coverage masks, completeness of our UV imaging catalogues, variations in redshift completeness, redshift distribution as a function of sky position, and redshift blunder rate. In Section 3 we describe our power spectrum calculation and its correction for redshift blunders. We compare the predictions of cosmological models to the resulting power spectra in Section 4 and itemize our conclusions in Section 5. We note that we construct our selection function for a fiducial flat Λ CDM cosmological model with matter density $\Omega_m = 0.3$.

2 WIGGLEZ SURVEY SELECTION FUNCTION

An overview of the WiggleZ Survey observing strategy and galaxy selection criteria is presented by Blake et al. (2009) and Drinkwater et al. (2010) and summarized in Table 1. Briefly, targets are chosen by a joint selection in UV and optical wavebands, using observations by the Galaxy Evolution Explorer satellite (GALEX) matched with ground-based optical imaging. A series of magnitude and colour cuts is used to preferentially select high-redshift star-forming galaxies with bright emission lines, which are observed using the AAOmega multi-object spectrograph at the Anglo-Australian Telescope (AAT).

The survey selection function $W(\vec{x})$ expresses the expected mean density of galaxies with spectroscopic redshifts at position \vec{x} , given the angular and luminosity survey selection criteria. An accurate determination of the selection function is essential in order to estimate the power spectrum, which describes the amplitude of fluctuations relative to the mean density.

Determination of the WiggleZ survey selection function is complicated by several factors, which are discussed in the following sub-sections:

- The boundaries of each survey region are determined by the overlapping network of UV and optical imaging coverage [see Section 2.1].
- The magnitude cuts used to select galaxies from the input imaging lie close to the faint completeness thresholds of those surveys. For example, the completeness of the GALEX UV data at the survey flux threshold varies with the amount of Galactic foreground dust, inducing a variation in target density with angular position [see Section 2.2].
- The spectroscopic redshift completeness of each AAOmega pointing (i.e. the fraction of observed spectra producing successful redshifts) varies considerably with observing conditions such as astronomical seeing and cloud cover, inducing a variation in the density of successful redshifts with angular position [see Section 2.3].
- The program of GALEX imaging has proceeded simultaneously with the spectroscopic follow-up at the AAT. The expansion of the angular mask of the survey with time must be tracked in order to properly model the angular density of redshifts [see Section 2.3].
- The spectroscopic redshift completeness of each AAOmega pointing varies systematically across the spectrograph field-of-view, decreasing towards the edges where acquisition errors are amplified [see Section 2.4].
- Whilst the survey is unfinished, the optical magnitude distribution of observed galaxies varies with position on the sky owing to the target prioritization scheme used for the observations (Drinkwater et al. 2010). This implies that the galaxy redshift distribution also varies with angular position [see Section 2.5].
- A fraction of the assigned galaxy redshifts are “blunders” resulting from emission-line mis-identifications. The rate of blunders depends on redshift, and hence distorts the true radial galaxy distribution [see Section 2.7].

2.1 Coverage masks

This part of the selection function establishes a (0,1) binary

Table 1. Summary of the WiggleZ Survey galaxy selection criteria.

UV magnitude cut	$NUV < 22.8$
Optical magnitude cut	$20 < r < 22.5$
UV colour cut	FUV dropout or $FUV - NUV > 1$
Optical-UV colour cut	$-0.5 < NUV - r < 2$
Optical colour cut	If $g < 22.5$ and $i < 21.5$, then $(r - i) < (g - r - 0.1)$ and $(r - i) < 0.4$

angular coverage mask indicating the availability of input targets.

The boundaries of each WiggleZ survey region are defined by the coverage maps of the UV and optical imaging data within that region. The UV data consists of a series of pointings of the GALEX satellite. The GALEX field-of-view is a circle of radius 0.6 deg; we select sources from a slightly smaller radius of 0.55 deg due to concerns about the GALEX photometry at the edges of the field (Morrissey et al. 2007). For the survey regions analyzed in this paper, the optical coverage map corresponds to the 4th Data Release of the SDSS.

The GALEX source catalogues contain small regions of bad data corresponding to scattered light from bright stars adjacent to the field-of-view. We inspect each GALEX field by eye for the presence of these artefacts and define rectangular masks to remove this bad data. These masks encompass a negligible fraction ($< 1\%$) of the survey area.

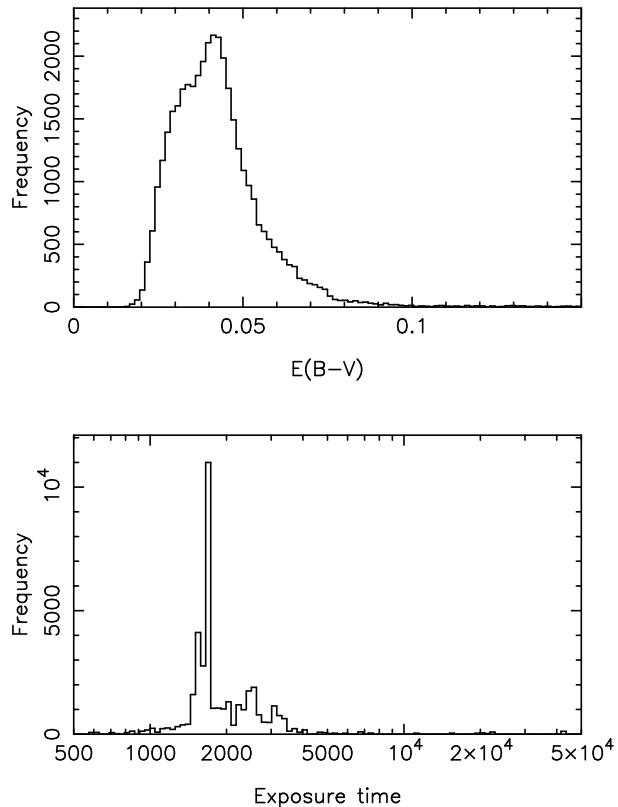
2.2 Variation of parent density with dust and exposure time

This part of the selection function modulates the angular coverage map in accordance with incompleteness in the parent imaging catalogues.

The faint UV magnitude threshold for WiggleZ survey selection, $NUV = 22.8$, is comparable to the magnitude completeness limit of the GALEX Medium Imaging Survey (MIS) which provides the targets. The incompleteness of the WiggleZ target catalogue is therefore significant and must be modelled in our selection function, because it determines the baseline target density on the sky in the absence of clustering. We calibrated this incompleteness factor as a function of foreground Galactic dust (quantified by the value of E_{B-V}) and GALEX exposure time t_{exp} .

The variations of E_{B-V} and t_{exp} across the survey regions analyzed in this paper are displayed in Figure 1. The distribution of exposure time is peaked in the range $1400 < t_{\text{exp}} < 1800$ sec (the canonical MIS exposure time is 1500 sec, equivalent to one orbit of the GALEX satellite when overheads are included). However, our analysis also includes fields with lower exposure times $500 < t_{\text{exp}} < 1400$ sec for which we are still gathering data. In addition some fields have significantly larger values of t_{exp} if they have been observed as part of other GALEX projects. The distribution of dust extinction is broad, peaking at $E_{B-V} \approx 0.04$. Although we correct the UV magnitudes for dust extinction (by an amount $A_{NUV} \approx 8E_{B-V} \approx 0.3$, see Drinkwater et al. 2010), the proximity of our observations to the MIS magnitude threshold induces a variation of completeness with E_{B-V} .

We used the GALEX NUV (dust-corrected) differential source counts (i.e., counts of galaxies in NUV magni-

**Figure 1.** Histograms of the values of GALEX exposure time and Galactic dust extinction across the WiggleZ survey regions analyzed in this paper.

tude bins) to calibrate the dependence of the WiggleZ survey completeness on E_{B-V} and t_{exp} . For this analysis we created a GALEX-SDSS matched galaxy sample for which we did not impose any of the WiggleZ survey magnitude or colour cuts. This is because the WiggleZ selection cuts reduce the target density by a factor of approximately 6, greatly increasing the noise in these measurements. We matched the GALEX NUV catalogues with the SDSS data (using a tolerance of 2.5 arcsec) and removed objects flagged as stars in SDSS. The presence of these stars would distort the galaxy number counts and induce spurious correlations with E_{B-V} owing to the non-uniform stellar distribution.

We constructed the source count by dividing the survey coverage map into small pixels of size 0.1×0.1 deg and assigning each pixel a mean value of E_{B-V} and t_{exp} . We then added up the pixel source counts in bins of E_{B-V} and t_{exp} .

Figure 2 illustrates the source count in bins of exposure time, restricting the analysis to pixels with low dust extinction ($E_{B-V} < 0.04$) in order to isolate the variation with

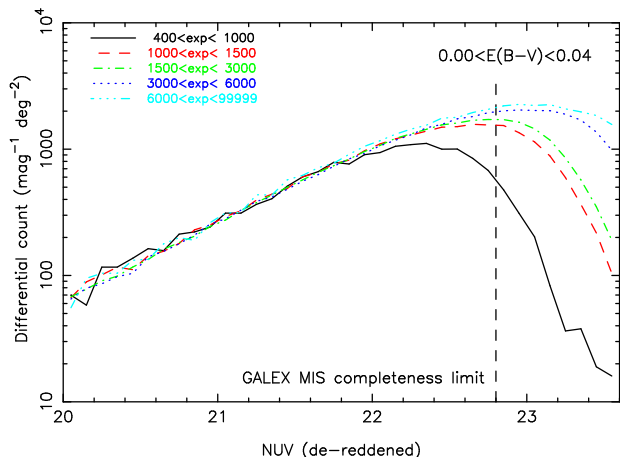


Figure 2. Differential source counts of GALEX-SDSS galaxy matches in bins of GALEX exposure time. We restrict the analysis to regions of the survey with low dust extinction $E_{B-V} < 0.04$. We note that the uppermost curve with the caption “6000 < exp < 99999” corresponds to the “fiducial” source count in the limit of low dust extinction and high GALEX exposure time, as discussed in the text.

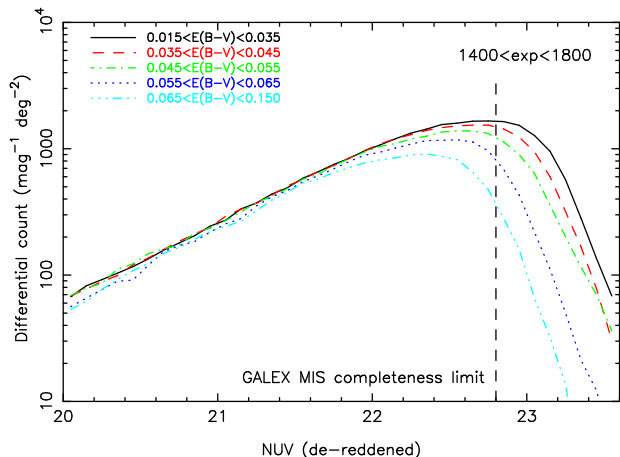


Figure 3. Differential source counts of GALEX-SDSS galaxy matches in bins of dust extinction. We restrict the analysis to regions of the survey with GALEX exposure times $1400 < t_{\text{exp}} < 1800$ sec.

exposure time. We expect to see the number counts rising with increasing magnitude (in the classic Euclidean regime, $d(\log_{10}N)/dm = 0.6$) and tailing off at faint magnitudes when incompleteness becomes significant. Indeed, Figure 2 illustrates that the counts in different exposure time bins agree well at bright magnitudes, and the completeness limit grows fainter with increasing exposure time. More detailed fits are presented below.

Figure 3 displays the counts in bins of E_{B-V} for GALEX observations in the exposure time range $1400 < t_{\text{exp}} < 1800$ sec, in order to isolate the variation with dust extinction. Again, the agreement is good at bright magnitudes (i.e. there is no significant residual dependence of the number counts on dust extinction) and the incompleteness at faint magnitudes increases with the value of E_{B-V} .

We found that a good fitting formula for these source

counts as a function of de-reddened magnitude $m = NUV$ is a power-law modulated by an incompleteness function:

$$\frac{dN}{dm}(m) = \frac{dN_0}{dm}(m) \times C(\mu, \sigma, m) \quad (1)$$

where

$$\frac{dN_0}{dm}(m) = 10^{\alpha+m\beta} \quad (2)$$

$$C(\mu, \sigma, m) = 0.5 \left[1 + \text{erf} \left(\frac{\mu - m}{\sigma} \right) \right] \quad (3)$$

where $\text{erf}(x)$ is the error function:

$$\text{erf}(x) = \frac{2}{\sqrt{\pi}} \int_0^x \exp(-t^2) dt \quad (4)$$

We first fitted Equation 1 to the source counts for survey regions in the ranges $E_{B-V} < 0.04$ and $t_{\text{exp}} > 6000$ sec, which we designated the “fiducial” source count $C_0(\mu_0, \sigma_0, m)$ in the limit of low dust extinction and high GALEX exposure time. The apparent incompleteness in this measurement is not due to GALEX observations but to the limiting magnitude threshold of the SDSS data with which we match the GALEX sources. We fitted the model to the magnitude range $20.0 < NUV < 22.8$ (motivated by the faint flux threshold for WiggleZ target selection). The best-fitting parameters for the fiducial source count are $\beta = 0.625 \pm 0.013$, $\mu_0 = 22.98 \pm 0.05$ and $\sigma_0 = 1.1 \pm 0.1$, which we assumed for the rest of this analysis. The errors in each parameter are quoted after marginalizing over the remaining parameters. Our derived number counts are consistent with Xu et al. (2005), who show that a model incorporating luminosity evolution provides a good fit to this data. We note that the overall amplitude of the number counts, parameterized by α in Equation 2, is not required for determining the incompleteness, as explained below.

We then defined the incompleteness in the GALEX catalogues as a function of E_{B-V} and t_{exp} , relative to these fiducial counts, by fitting the model:

$$\frac{dN}{dm}(m) = \frac{dN_0}{dm}(m) \times C_0(\mu_0, \sigma_0, m) \times C(\mu, \sigma, m) \quad (5)$$

By construction, $C = 1$ in the limit of low dust extinction and high exposure time. We found that the best-fitting value of σ does not vary significantly with dust or exposure time. Therefore we fixed $\sigma = 0.578$ such that the completeness function depended on just one parameter, μ . We then fitted the value of μ as a function of both E_{B-V} and t_{exp} ; the results are displayed in Figure 4, together with the error in μ obtained by marginalizing over the other fitted parameters.

We can compare these results to theoretical expectations. The variation of the completeness limit μ with t_{exp} (at fixed E_{B-V}) agrees well with the theoretical expectation for background-limited imaging of fixed signal-to-noise, in which a doubling of exposure time equates to approximately 0.4 magnitudes of survey depth. The variation of μ with E_{B-V} (at fixed t_{exp}) should follow the dust-extinction law $\Delta\mu \approx 8\Delta E_{B-V}$. The observed slope in Figure 4 is in fact a little steeper, owing to the influence of the additional factor $C_0(m)$ in Equation 5.

The completeness of the GALEX-SDSS parent catalogue for the UV flux threshold $m_0 = 22.8$ can be determined for a given $\mu(t_{\text{exp}}, E_{B-V})$ by evaluating

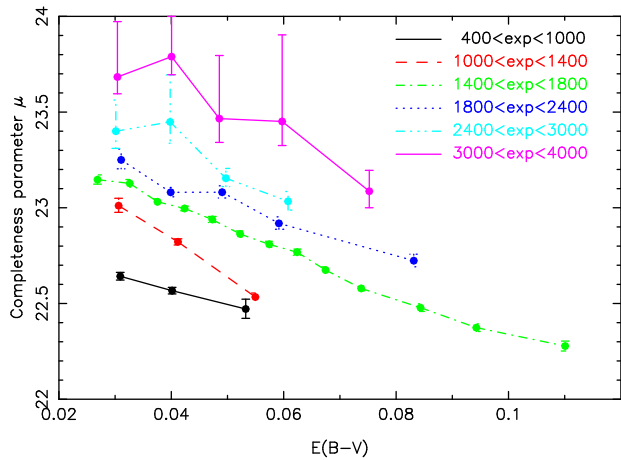


Figure 4. Dependence of the completeness parameter μ on dust extinction, in bins of exposure time. The measurements of μ are of highest quality for the dominant exposure time range $1400 < t_{\text{exp}} < 1800$ sec. The error range in μ is asymmetric about the best-fitting value because the model becomes increasingly insensitive to μ as the value of μ increases. The measurement for each dust bin is plotted at the median value of E_{B-V} for that bin.

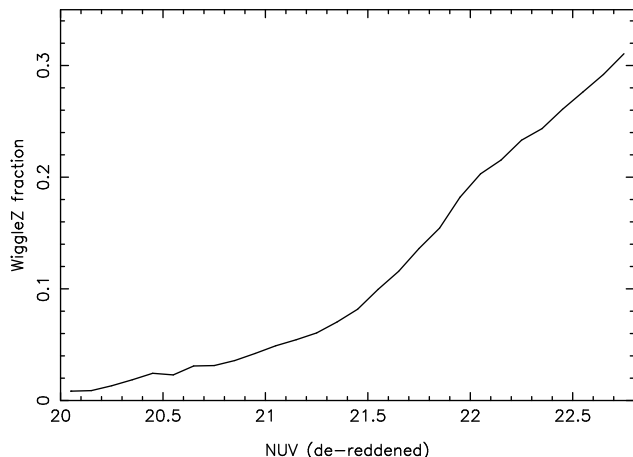


Figure 5. Fraction of GALEX-SDSS matches that are selected as WiggleZ targets as a function of GALEX NUV magnitude.

$$\text{Completeness}(\mu) = \frac{\int_0^{m_0} \frac{dN_0}{dm} C_0(\mu_0, \sigma_0, m) C(\mu, \sigma, m) dm}{\int_0^{m_0} \frac{dN_0}{dm} C_0(\mu_0, \sigma_0, m) dm} \quad (6)$$

In order to model the WiggleZ survey target density from these completeness measurements we must now allow for the fraction of GALEX-SDSS matched sources that are selected as WiggleZ targets as a function of NUV magnitude. This function is plotted in Figure 5. WiggleZ targets are preferentially faint in NUV owing to the colour selection cut $-0.5 < NUV - r < 2$. We weighted Equation 6 with this function in order to determine the WiggleZ survey angular completeness map. We defined this map using a uniform grid of pixels in right ascension and declination.

In Figure 6 we compare the WiggleZ target densities as a function of dust extinction predicted by our number-counts modelling with the densities observed in the catalogue. We plot the percentage difference of the measured density from

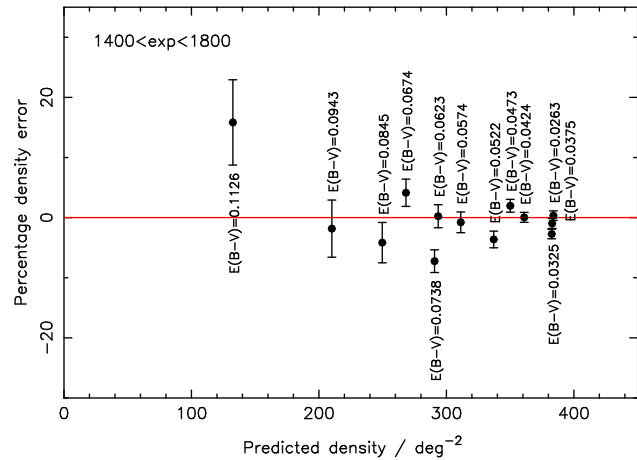


Figure 6. Comparison of the observed and modelled target density for the WiggleZ catalogue in bins of dust extinction for the GALEX exposure time range $1400 < t_{\text{exp}} < 1800$ sec. The average value of E_{B-V} for each dust bin is displayed next to the corresponding data point. Poisson error bars, which are likely to be a mild under-estimate of the true error, are shown for the measured density.

the predicted density. The good match indicates that our selection function model is successful. An example parent catalogue completeness map for the 9-hr survey region is displayed as a panel in Figure 7.

We note that the variation in the angular density of targets is dominated by incompleteness in the UV imaging data rather than in the optical imaging data. Although the faint optical magnitude threshold for WiggleZ selection ($r = 22.5$) lies at the completeness limit of the SDSS, the $NUV - r$ colour selection cut implies that the median r -band magnitude of WiggleZ targets is $r \approx 21.5$ and the variation of SDSS completeness with E_{B-V} is negligible. We also studied the variation of completeness with the local astronomical seeing in the SDSS images, and found no significant effect on the target densities.

2.3 Redshift completeness map

This part of the selection function samples the density map of the parent target catalogue with the pattern of spectroscopic follow-up observations.

The spectroscopic observations of the WiggleZ survey are defined by a series of AAT pointing centres across each survey region. The pointing centres for each region are determined prior to each survey observing run based upon the available distribution of targets at the time, using a “simulated annealing” algorithm. Each patch of sky must be observed three to four times on average to build up the WiggleZ redshift catalogue, therefore we obtain a series of overlapping pointings. Each individual pointing results in a fraction of successful redshifts which varies considerably with astronomical seeing, airmass and cloud cover from under 40% in poor conditions (> 2.5 arcsec seeing or airmass $\sec(z) > 1.5$ or $> 2/8$ ths cloud) to over 80% in good conditions (< 1.5 arcsec seeing and $\sec(z) < 1.4$ and no cloud). Furthermore, the fraction of successful redshifts in any pointing varies across the field plate of the 2dF spectrograph, as discussed in

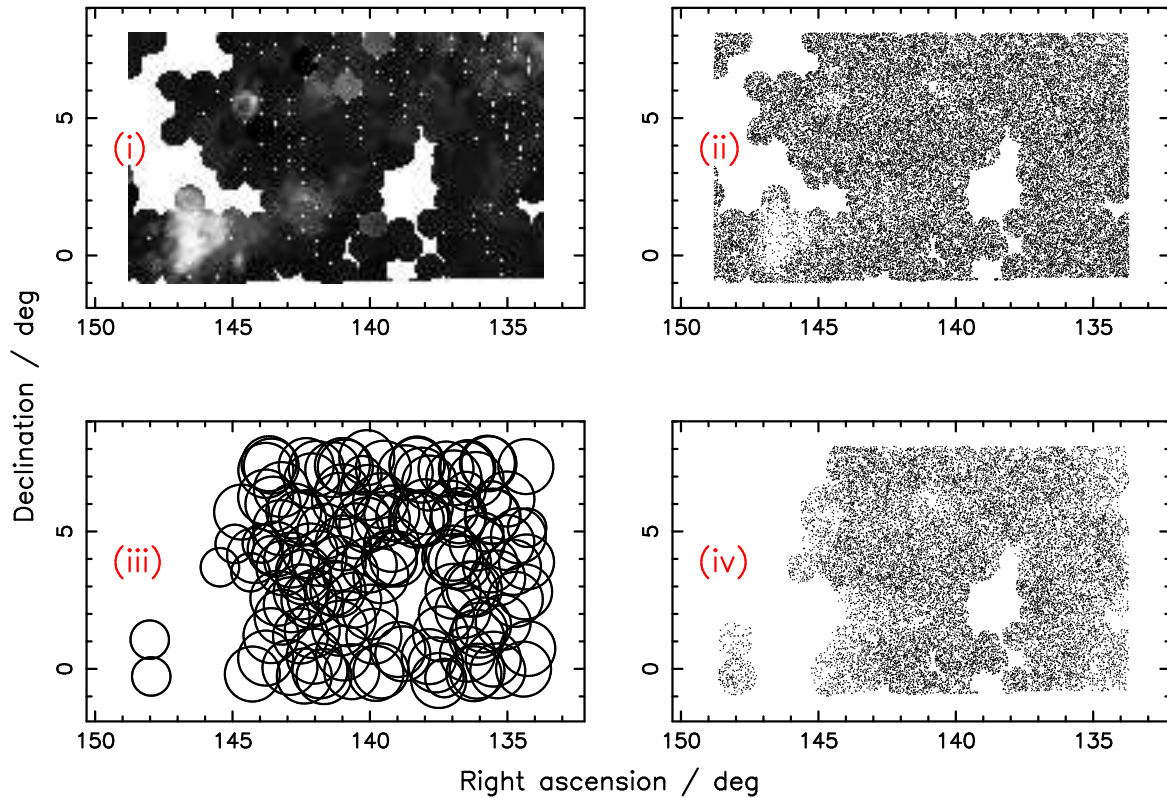


Figure 7. Panels showing for the WiggleZ 9-hr region: (i) the angular completeness map of the parent catalogue, (ii) a realization of the parent catalogue sampled from this map, (iii) the sequence of 2dF field centres, (iv) a realization of the redshift catalogue. Note in panel (iii) that in some pointings of the survey a field radius of 0.7 deg rather than 1.0 deg was used, due to concerns over radial-dependent redshift completeness within 2dF pointings.

more detail below. Therefore, as the survey is still partially complete, the redshift completeness map is a complicated function of position on the sky.

We determined the redshift completeness function in each survey region using Monte Carlo realizations of the observations. The steps in the construction of a realization are illustrated in Figure 7. For each region we started with the density map as a function of dust and exposure time created by the process described in Section 2.2 [Figure 7, panel (i)]. We created a Monte Carlo realization of this density map, containing the same number of galaxies as the real target catalogue, by first generating a uniform random catalogue and then excluding points based on a probability equal to the local incompleteness [Figure 7, panel (ii)]. The spectroscopic observations consist of a series of overlapping AAT pointings [Figure 7, panel (iii)]. Each pointing was applied to our realization by laying down a field circle at the correct angular position and randomly assigning the appropriate number of observed sources to spectroscopic fibres.

We note that the available target area has grown over the duration of the survey because the GALEX imaging observations are proceeding simultaneously with the redshift follow-up. In the Monte Carlo simulations it is therefore necessary to track the distribution of GALEX tiles available prior to each WiggleZ observing run and only assign target sources to each random realization in areas that were available at the time of each pointing.

For each telescope pointing in the random realization,

a fraction of the observed sources are flagged with successful redshifts. The remainder are flagged with unsuccessful redshifts. The total number of successful redshifts for each pointing in the Monte Carlo realization is equal to that achieved in the corresponding survey observation. The probability of a given random source being assigned a successful redshift varies across the field-of-view of the pointing in the manner described below in Section 2.4. The resulting random realization, constructed by applying the full set of pointings, is displayed in Figure 7, panel (iv).

The WiggleZ survey observing strategy involves obtaining repeat spectra of unsuccessful redshifts observed in poor conditions. In addition, a small number of galaxies with existing successful redshifts are re-observed in order to quantify the redshift blunder rate. Each of these categories of observation are included when constructing the Monte Carlo realizations.

2.4 Variation of redshift completeness across the spectrograph field-of-view

The probability of obtaining a successful redshift in a WiggleZ survey pointing depends on the source position within the spectrograph field-of-view. We find that galaxies observed at the edges of the field plate have a reduced redshift completeness because these observations are more seriously affected by rotational mis-alignments in target acquisition,

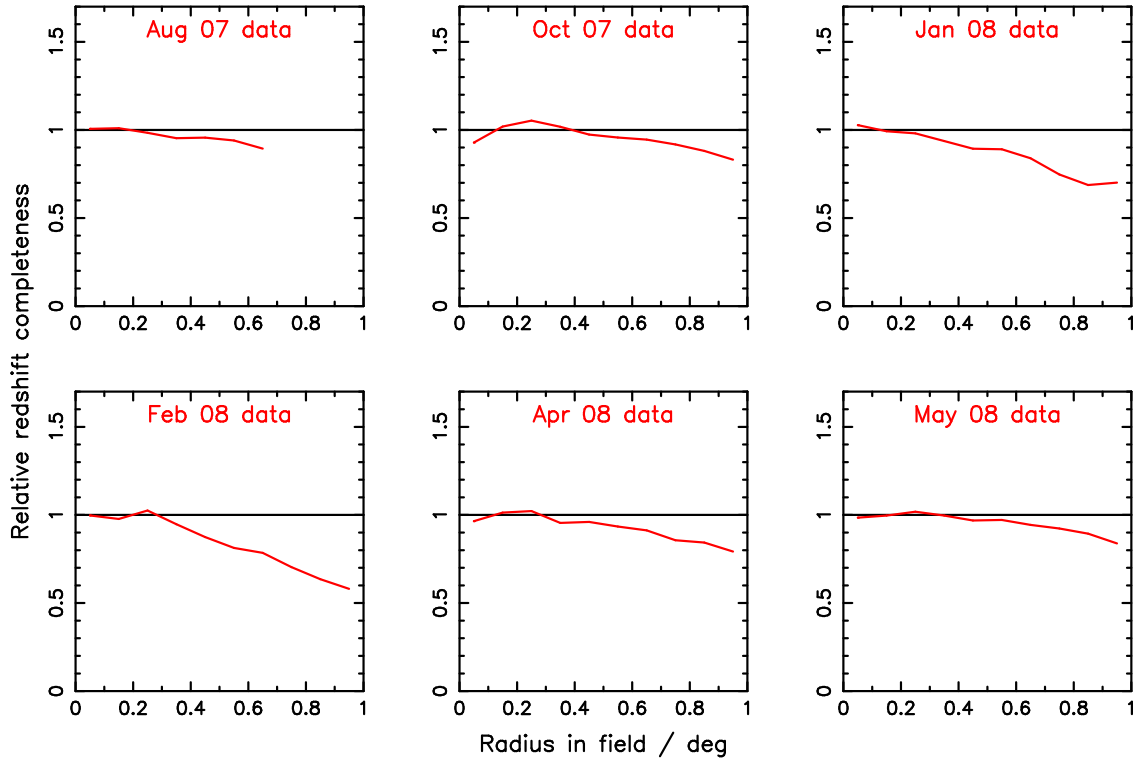


Figure 8. Radial dependence of the redshift completeness in the 2-degree field for the six WiggleZ survey observing runs between August 2007 and May 2008. In August 2007 the field of observation was restricted to radii < 0.7 degrees. We note that the completeness is normalized relative to a level of 1.0 at the centre of each field.

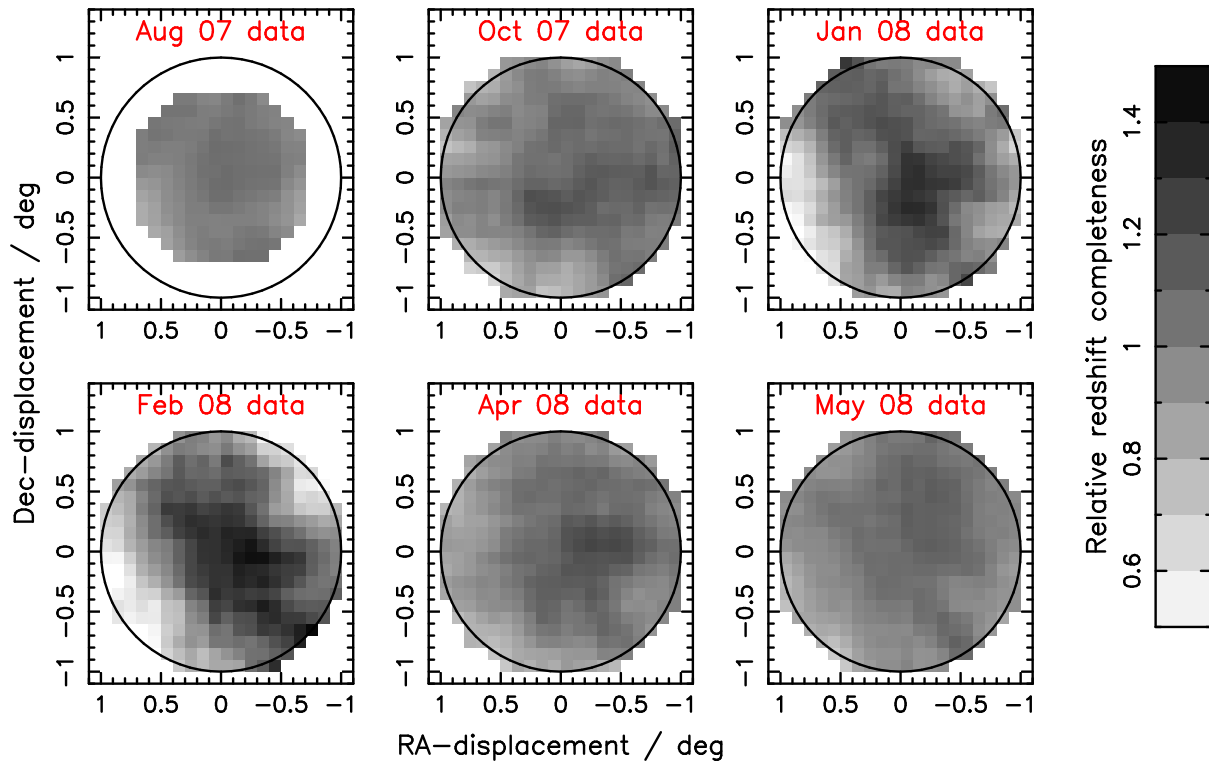


Figure 9. Dependence of the redshift completeness on position in the 2-degree field for the six WiggleZ survey observing runs between August 2007 and May 2008. In August 2007 the field of observation was restricted to radii < 0.7 degrees. We note that the completeness is normalized relative to a mean level of 1.0 averaged across each field.

which is performed using a limited number of guide-fibre bundles.

Furthermore, we find that the pattern of redshift completeness across the field-of-view varies between survey observing runs as the spectrograph set-up is re-calibrated, but remains stable throughout an observing run. Although individual fibres can be placed in the field-of-view by the 2dF robot positioner with an accuracy of $20\mu\text{m}$ (0.3 arcsec), systematic errors can develop in the mapping of (x, y) position on the field plate to (R.A., Dec.) position on the sky. These errors are caused by minor discrepancies in the atmospheric correction applied to target apparent positions, and (at times during the survey) by an instability in the modelling of opto-mechanical distortions between the prime focus corrector and the 2dF field plates. These additional errors imply that the redshift completeness variation is not radially symmetric.

These effects are illustrated by Figures 8 and 9. In Figure 8 we display the radial variation in redshift completeness for WiggleZ survey observing runs between August 2007 and May 2008. Figure 9 displays the 2D variation of redshift completeness across the field plate for each of these observing runs, and we use these 2D maps to generate the probabilities of successful redshifts in the Monte Carlo realizations described above. In some observing runs, such as August 2007, we restricted our spectroscopic observations to the central 0.7 deg radius of the 1-deg radius field-of-view of the 2dF spectrographs, because the drop in redshift completeness at the edges of the field was particularly significant.

2.5 Radial selection function versus angular position

This part of the selection function creates the appropriate radial distribution of galaxies depending on the distribution of r -band magnitudes in each 2dF pointing.

The final step in the creation of the Monte Carlo realizations is to assign a random redshift to each galaxy, thus establishing the selection function in the radial direction. Targets in the WiggleZ survey are prioritized for observation in accordance with their SDSS r -band magnitudes such that the faintest galaxies are observed earliest in the sequence (Drinkwater et al. 2010). In detail we use five priority bands which divide the magnitude range $20.0 < r < 22.5$ into equal pieces. Given that there is a correlation between redshift and magnitude, this implies that the survey redshift distribution varies across the sky in a manner dependent on the density of redshifts obtained in a given area.

We track this in our random catalogues by recording for each telescope pointing the number of successful redshifts obtained in each magnitude priority band, and assigning these magnitude identifications to sources in the random catalogues. We note that the weak dependence of redshift completeness on r -band magnitude is also absorbed into this step of the process.

For each magnitude band we measured the redshift distribution $N(z)$ of successful redshifts using the existing WiggleZ spectroscopic data. In order to reduce the fluctuations due to cosmic variance, we combined the data for the 9-hr, 11-hr and 15-hr survey regions in this analysis. We used these probability distributions to assign redshifts to random sources on the basis of their magnitude. Figure 10 plots $N(z)$

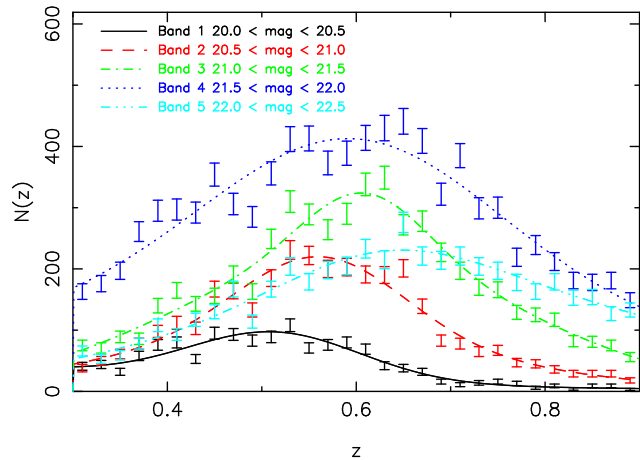


Figure 10. The distribution of WiggleZ redshifts z in the five magnitude bands in which the targets are prioritized. Data is shown for the combined 9-hr, 11-hr and 15-hr survey regions for the redshift range $0.3 < z < 0.9$ analyzed in this paper. Poisson error bars are shown for the points and the data is fitted with a sum of two Gaussian functions.

for the five magnitude bands for the combined WiggleZ regions. We fit the redshift distributions with a sum of two Gaussian functions and sample the random redshifts from these smooth distributions. Future work will establish $N(z)$ from measurements of the galaxy luminosity function instead.

2.6 Final construction of the survey selection function

The method described in the preceding sub-sections allows us to construct Monte Carlo realizations for each WiggleZ region incorporating the angular and radial variations of the selection function. We can accurately determine the full selection function function $W(\vec{x})$ by stacking together many such realizations: we typically generate 10,000 realizations for each region. We pixelize the selection function in grid cells corresponding to our power spectrum measurement, as discussed in Section 3.1. When converting redshifts to distances we use a fiducial flat Λ CDM cosmological model with matter density $\Omega_m = 0.3$.

2.7 Redshift blunder rate

The redshifts of galaxies in the WiggleZ survey are typically based on identifications of emission lines; the signal-to-noise of the spectra is usually too low to permit detection of the galaxy continuum. The principal line used for redshift identification is the [OII] doublet at rest-frame wavelength 3727\AA . This emission line lies in our observed spectral window $4700 - 9500\text{\AA}$ for the galaxy redshift range $0.26 < z < 1.55$. The redshift identification is confirmed for most galaxies by the additional presence of emission lines such as $H\beta$ 4861\AA , [OIII] 4959\AA , [OIII] 5007\AA , and $H\alpha$ 6563\AA (Drinkwater et al. 2010).

However, not all redshift identifications are based on multiple emission lines. Features redward of [OII] progressively leave the observed spectral range with increasing red-

shift. The $H\beta$ and $H\alpha$ lines are observable for the ranges $z < 0.95$ and $z < 0.45$, respectively. At relatively high redshifts the galaxy emission lines must be identified against a background of noisy sky emission lines. Despite these difficulties, we can gain some confidence in single-line redshifts based on [OII] either through detection of the doublet, which is marginally possible with our spectral resolution for galaxies lying at $z > 0.8$, or by eliminating other solutions by failure to detect [OII] at lower wavelengths in cleaner parts of the spectrum.

We assign quality flags from $Q = 1$ (lowest) to $Q = 5$ (highest) for each WiggleZ redshift based on the confidence of our measurement. Redshifts with quality $Q \geq 3$ are considered “reliable” and used in our analysis. Redshifts with quality $Q \geq 4$ are based on multiple emission lines and are very secure. Galaxies with redshifts based on noisy data or single emission lines are assigned $Q = 3$. The fraction of reliable redshifts with $Q = 3$ is approximately one-third.

Some fraction of WiggleZ redshifts will be blunders. We distinguish two types of redshift blunder for the purposes of our analysis. Firstly, a galaxy emission line may be mis-identified as another, incorrect, emission line. In our power spectrum measurement this represents (approximately) a convolution of the galaxy density field whereby structures at a given redshift are coherently copied to a second redshift. Secondly, a night-sky emission line may be mis-identified as a galaxy emission line. As there are a large number of night-sky emission lines available for mis-identification, this effectively corresponds to a randomizing of the galaxy density field through the addition of objects whose positions are uncorrelated with the underlying density.

We studied the redshift blunder rate through a programme of repeat observations. In each survey pointing we assigned a small number of spectrograph fibres (typically 3-5) to galaxies which have already been assigned redshifts with quality $Q \geq 3$. We define two redshifts as inconsistent if they differ by $\Delta z > 0.002$ (the typical redshift error for our spectra is $\Delta z = 0.0005$ or 100 km s^{-1}).

We find that pairs of repeat galaxy redshifts which both possess quality $Q \geq 4$ disagree in 2% of cases. Assuming that one of the pair of inconsistent values is the correct redshift, this implies that the blunder rate for the set of $Q \geq 4$ redshifts is 1%. Pairs of repeat redshifts which both possess $Q = 3$ disagree in $31 \pm 2\%$ of cases. However, we can obtain a larger statistical sample for analysis if we consider pairs composed of $Q = 3$ and $Q \geq 4$ redshifts, supposing that the higher quality redshift is the correct value. Under this method we find that the blunder rate of $Q = 3$ redshifts is $17 \pm 1\%$, in good agreement with the internal blunder rate for $Q = 3$ pairs. Given that approximately one-third of reliable redshifts are assigned $Q = 3$, the overall blunder rate for the WiggleZ survey is about 5%. However, we must carefully quantify the redshift blunders in more detail in order to obtain an unbiased measurement of the galaxy power spectrum.

In Figure 11 we illustrate the fraction of redshift blunders resulting from the mis-identification of an emission line with a second, incorrect, emission line by plotting the distribution of values of $(1+z_1)/(1+z_2)$ for inconsistent repeat redshifts composed of $Q = 3$ and $Q \geq 4$ pairs. The values of (z_1, z_2) are the redshifts of the $Q = 3$ and $Q \geq 4$ spectra, respectively. This histogram reveals three signifi-

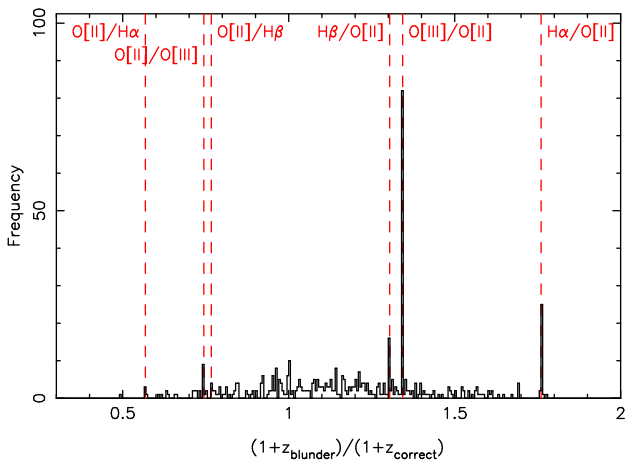


Figure 11. Distribution of values of $(1+z_1)/(1+z_2)$ for inconsistent repeat redshifts derived from pairs of spectra with quality flags $Q = 3$ (redshift z_1) and $Q \geq 4$ (redshift z_2). The vertical lines indicate the ratios expected in the cases where $H\beta$, [OIII] and $H\alpha$ are mis-identified as [OII].

cant spikes corresponding to the mis-identification of $H\beta$, [OIII] 5007\AA and $H\alpha$ as [OII]. Approximately 30% of redshift blunders correspond to this type of mis-identification; the correct redshift in such cases is typically lower than the blunder redshift.

Figure 12 plots the distribution of redshift blunders not contained in the three spikes in Figure 11. This type of blunder, comprising about 70% of all blunders, corresponds to mis-identification of sky emission lines as [OII]. In Figure 12 we have also fitted a model for the redshift distribution $N(z)$ of the form:

$$N(z) \propto \left(\frac{z}{z_0}\right)^\alpha \exp\left[-\left(\frac{z}{z_0}\right)^\beta\right]. \quad (7)$$

The best-fitting parameters are $z_0 = 1.11$, $\alpha = 1.24$, $\beta = 6.46$. We note that the distribution of blunders peaks at a significantly higher redshift than the distribution of correct redshifts shown in Figure 10. This implies that the blunder fraction varies significantly with redshift – this behaviour is plotted in Blake et al. 2009, figure 6. In Section 3.2 we model the effect of these types of redshift blunders on measurements of the galaxy power spectrum.

3 POWER SPECTRUM ANALYSIS

3.1 Power spectrum estimation methodology

In this Section we summarize our method of power spectrum estimation, prior to presenting our analysis of the WiggleZ survey data in Section 3.3. Our power spectrum estimation is based on the optimal weighting scheme of Feldman, Kaiser & Peacock (1994) [FKP] (also see the discussions in Tadros & Efstathiou 1996; Hoyle et al. 2002). When converting redshifts to distances we use a fiducial flat Λ CDM cosmological model with matter density $\Omega_m = 0.3$. We first enclosed the survey cone for the particular region and redshift interval within a cuboid of sides (L_x, L_y, L_z) and gridded the galaxy catalogue in cells numbering (n_x, n_y, n_z) using nearest grid point (NGP) assignment to produce a distribution $n(\vec{x})$. The

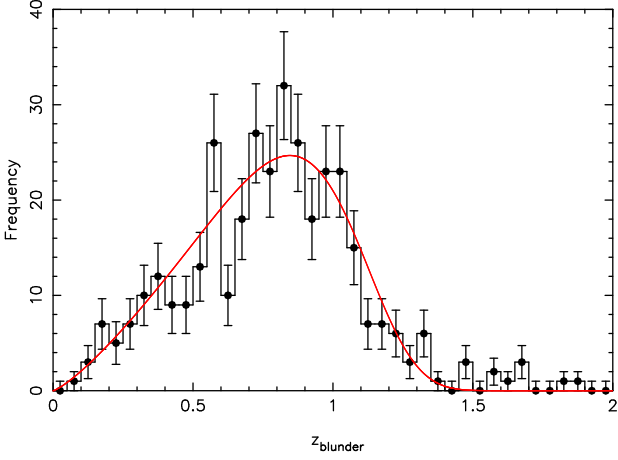


Figure 12. The distribution of redshift blunders for the pairs in Figure 11 which do not lie in the three prominent spikes. The solid line is the best fit of the model described by Equation 7.

cell dimensions were chosen such that the Nyquist frequencies in each direction (e.g. $k_{\text{Nyq},x} = \pi n_x / L_x$) exceeded the maximum frequency of measured power k_{max} by at least a factor of two (although we corrected for the effect of NGP assignment on the power spectrum as explained below).

We then applied a Fast Fourier transform to the grid of data, weighting each pixel by a factor $w(\vec{x})$ following the method of FKP:

$$\tilde{n}(\vec{k}) = \sum_{\vec{x}} n(\vec{x}) w(\vec{x}) \exp(i\vec{k} \cdot \vec{x}) \quad (8)$$

where the weighting factor is given by

$$w(\vec{x}) = \frac{1}{1 + W(\vec{x}) N_c n_0 P_0} \quad (9)$$

(FKP, equation 2.3.4). In Equation 9, $N_c = n_x n_y n_z$ is the total number of grid cells, $n_0 = N/V$ is the mean number density of galaxies in units of $h^3 \text{Mpc}^{-3}$, where N is the total number of galaxies and $V = L_x L_y L_z$ is the cuboid volume, and P_0 is a characteristic value of the power spectrum at the Fourier wavenumber of interest. The purpose of the weighting scheme of Equation 9 is give equal weight per volume where we are limited by cosmic variance, and equal weight per galaxy where we are limited by shot noise, resulting in an optimal measurement of the power spectrum amplitude $P(k)$ in the case where $P(k) \approx P_0$.

In Equation 9, $W(\vec{x})$ is proportional to the survey selection function determined in Section 2, which describes the number of galaxies expected in each cell \vec{x} in the absence of clustering. We assume here the normalization

$$\sum_{\vec{x}} W(\vec{x}) = 1. \quad (10)$$

We note that summations over cells \vec{x} may be related to the equivalent integration over volume elements $d^3\vec{x}$ by

$$\frac{1}{N_c} \sum_{\vec{x}} W(\vec{x}) = \frac{1}{V} \int W(\vec{x}) d^3\vec{x}. \quad (11)$$

We also apply a Fast Fourier transform to the survey selection function:

$$\tilde{W}(\vec{k}) = \sum_{\vec{x}} W(\vec{x}) w(\vec{x}) \exp(i\vec{k} \cdot \vec{x}) \quad (12)$$

The estimate of the galaxy power spectrum for wavenumber \vec{k} is then

$$P_{\text{est}}(\vec{k}) = \frac{|\tilde{n}(\vec{k}) - N\tilde{W}(\vec{k})|^2 - N \sum_{\vec{x}} W(\vec{x}) w^2(\vec{x})}{N^2 N_c \sum_{\vec{x}} W^2(\vec{x}) w^2(\vec{x})} \quad (13)$$

This estimate of the power spectrum is biased by the process of NGP assignment (Jing 2005). In order to remove this bias we calculated the correction factor for each Fourier mode (by which the power spectrum estimate should be divided):

$$\text{Correction factor}(\vec{k}) = \frac{\sum_{\vec{m}} H^2(\vec{k}') P(\vec{k}')}{P(\vec{k})} \quad (14)$$

where $\vec{m} = (m_x, m_y, m_z)$ is a vector of integers, $\vec{k}' = (k'_x, k'_y, k'_z) = (k_x + m_x k_{\text{Nyq},x}, k_y + m_y k_{\text{Nyq},y}, k_z + m_z k_{\text{Nyq},z})$ and

$$H(\vec{k}) = \frac{\sin\left(\frac{\pi k_x}{2k_{\text{Nyq},x}}\right) \sin\left(\frac{\pi k_y}{2k_{\text{Nyq},y}}\right) \sin\left(\frac{\pi k_z}{2k_{\text{Nyq},z}}\right)}{\left(\frac{\pi k_x}{2k_{\text{Nyq},x}}\right) \left(\frac{\pi k_y}{2k_{\text{Nyq},y}}\right) \left(\frac{\pi k_z}{2k_{\text{Nyq},z}}\right)} \quad (15)$$

In Equation 14, $P(\vec{k})$ is the underlying model power spectrum. Given that this is initially unknown, we proceed by an iterative approach: we assume a fiducial cosmological model, compute the correction factor, fit cosmological parameters to the power spectrum, re-calculate the correction factor, and then repeat the parameter fit. The magnitude of the correction is typically 2% at scale $k \approx 0.2 h \text{Mpc}^{-1}$.

The spatially-varying selection function $W(\vec{x})$ has two effects on the process of power spectrum estimation. Firstly the expectation value of Equation 13 is the underlying power spectrum $P(\vec{k})$ convolved with the survey selection function:

$$\langle P_{\text{est}}(\vec{k}) \rangle = \frac{\sum_{\vec{k}'} P(\vec{k}') |\tilde{W}(\vec{k} - \vec{k}')|^2}{N_c \sum_{\vec{x}} W^2(\vec{x}) w^2(\vec{x})} \quad (16)$$

The numerator of Equation 16 is summed over the grid points \vec{k}' in Fourier space for which the Fast Fourier Transform of $W(\vec{x})$ is calculated, i.e. spaced by $(\Delta k_x, \Delta k_y, \Delta k_z) = (2\pi/L_x, 2\pi/L_y, 2\pi/L_z)$. For reasons of computing speed when fitting models, we re-cast this equation as a matrix multiplication in Fourier bins of width $\Delta k = 0.01 h \text{Mpc}^{-1}$:

$$\langle P_{\text{est}}(i) \rangle = \sum_j M_{ij} P_{\text{mod}}(j) \quad (17)$$

We determine the convolution matrix M_{ij} by evaluating the full sum of equation 16 for a set of unit vectors, e.g. for bin i :

$$P(\vec{k}) = 1 \quad (k_{i,\text{min}} < |\vec{k}| < k_{i,\text{max}}) \quad (18)$$

$$= 0 \quad \text{otherwise} \quad (19)$$

Secondly, the estimates of the power in different Fourier modes \vec{k} become correlated. If we average the estimates of Equation 13 into bins in Fourier space, labelling the bins by i , the covariance between bins i and j is given by

$$\langle \delta P_i \delta P_j \rangle = \frac{2}{N_{\vec{k}} N_{\vec{k}'}} \sum_{\vec{k}, \vec{k}'} |PQ(\vec{k} - \vec{k}') + S(\vec{k} - \vec{k}')|^2 \quad (20)$$

(FKP, equation 2.5.2) where \vec{k} and \vec{k}' are pairs of Fourier

modes lying in bins i and j , P is the characteristic power spectrum amplitude in bins i and j defined below, and the functions $Q(\vec{k})$ and $S(\vec{k})$ are given by FKP equations 2.2.3 and 2.2.5:

$$Q(\vec{k}) = \frac{\sum_{\vec{x}} W^2(\vec{x}) w^2(\vec{x}) \exp(i\vec{k}\cdot\vec{x})}{\sum_{\vec{x}} W^2(\vec{x}) w^2(\vec{x})} \quad (21)$$

$$S(\vec{k}) = \left(\frac{1}{n_0 N_c} \right) \frac{\sum_{\vec{x}} W(\vec{x}) w^2(\vec{x}) \exp(i\vec{k}\cdot\vec{x})}{\sum_{\vec{x}} W^2(\vec{x}) w^2(\vec{x})} \quad (22)$$

In deriving Equation 20 it is assumed that the power spectrum factor P which appears is effectively constant over Fourier separations $\vec{k} - \vec{k}'$ which produce correlated estimates. For our datasets the Fourier transform of the selection function, $\tilde{W}(\vec{k})$, is sufficiently compact around $k = 0$ that this is a valid approximation. We evaluated Equation 20 for each survey region by a direct summation over Fourier modes in the FFT grid. Equation 20 depends on the underlying power spectrum, which is initially unknown, in the same manner as equation 14. We again used an iterative approach whereby we initially used a default model power spectrum to make this calculation, and then replaced it using the fitted parameters.

In order to facilitate comparison with other studies it is useful to take the limit of these equations in the case where the selection function is constant, i.e. $W(\vec{x}) = 1/N_c$. The power spectrum estimator of Equation 13 becomes

$$P_{\text{est}}(\vec{k}) = \frac{|\tilde{n}(\vec{k}) - N\tilde{W}(\vec{k})|^2 - N}{N^2} \quad (23)$$

and the covariance matrix in Equation 20 reduces to a diagonal matrix with entries:

$$\langle (\delta P_i)^2 \rangle = \frac{2}{N_{\vec{k}}} \left(P + \frac{1}{n_0} \right)^2 \quad (24)$$

where $N_{\vec{k}}$ is the number of Fourier modes lying in bin i . Equation 24 clarifies that there are two sources of error in an estimate of the power spectrum: cosmic variance and shot noise, represented by the two terms inside the bracket.

3.2 Redshift blunder correction

In this Section we calculate the distortion in the galaxy power spectrum created by the types of redshift blunder described in Section 2.7. In order to gain intuition we begin with a simple model using the ‘‘flat-sky approximation’’ which supposes that galaxies are scattered in position along a single axis of the cuboid (which we take as the x -axis). Defining $\delta(\vec{x})$ as the galaxy overdensity in the cell at position $\vec{x} = (x, y, z)$, the galaxy number distribution is given by

$$n(\vec{x}) = NW(\vec{x})[1 + \delta(\vec{x})] \quad (25)$$

where $W(\vec{x})$ is the selection function normalized as above. We now suppose that a fraction f of galaxies are scattered in position along the x -axis such that their final x -position is drawn from a probability distribution $V(x)$ (i.e., as described by Equation 7 for our data). This process creates a scattered galaxy number distribution given by

$$S(\vec{x}) = N_1 V(x) \sum_{x'} n(x', y, z) \quad (26)$$

where the normalization constant N_1 can be calculated by requiring that $\sum_{\vec{x}} S(\vec{x}) = fN$. Equations 25 and 26 have Fourier transforms

$$\tilde{n}(\vec{k}) = N [\tilde{W}(\vec{k}) + \tilde{C}(\vec{k})] \quad (27)$$

$$\tilde{S}(\vec{k}) = fN\tilde{V}(k_x) [\tilde{W}(0, k_y, k_z) + \tilde{C}(0, k_y, k_z)] \quad (28)$$

where we have defined the convolved density field

$$\tilde{C}(\vec{k}) = \sum_{\vec{k}'} \tilde{W}(\vec{k}' - \vec{k}) \tilde{\delta}(\vec{k}') \quad (29)$$

It is convenient to subtract the selection function contribution:

$$\tilde{n}'(\vec{k}) = \tilde{n}(\vec{k}) - N\tilde{W}(\vec{k}) \quad (30)$$

$$\tilde{S}'(\vec{k}) = \tilde{S}(\vec{k}) - fN\tilde{W}(0, k_y, k_z)\tilde{V}(k_x) \quad (31)$$

We now construct the combined density field $m(\vec{x}) = (1 - f)n(\vec{x}) + S(\vec{x})$ and write (for the purposes of this calculation) a simple power spectrum estimator

$$P_{\text{est}}(\vec{k}) = \frac{|\tilde{m}'(\vec{k})|^2 - N}{N^2} \quad (32)$$

where $\tilde{m}'(\vec{k}) = (1 - f)\tilde{n}'(\vec{k}) + \tilde{S}'(\vec{k})$. The terms needed to determine $|\tilde{m}'(\vec{k})|^2$ are:

$$|\tilde{n}'(\vec{k})|^2 = (1 - f)^2 N^2 |\tilde{C}(\vec{k})|^2 \quad (33)$$

$$\tilde{n}'^*(\vec{k})\tilde{S}'(\vec{k}) = f(1 - f)N^2 \tilde{V}(k_x) P'(\vec{k}) \quad (34)$$

$$|\tilde{S}'(\vec{k})|^2 = f^2 N^2 |\tilde{C}(0, k_y, k_z)|^2 |\tilde{V}(k_x)|^2 \quad (35)$$

where

$$P'(\vec{k}) = \sum_{\vec{k}'} P(\vec{k}') \tilde{W}_{\vec{k}' - \vec{k}} \tilde{W}_{\vec{k}' - (0, k_y, k_z)}^* \quad (36)$$

Writing the convolved power spectrum as $P_c(\vec{k}) = |\tilde{C}(\vec{k})|^2$, the final result for the power spectrum estimate is:

$$P_{\text{est}}(\vec{k}) = (1 - f)^2 P_c(\vec{k}) + 2f(1 - f) \text{Re}[\tilde{V}(k_x) P'(\vec{k})] + f^2 P_c(0, k_y, k_z) |\tilde{V}(k_x)|^2 \quad (37)$$

In the special case that the selection function and scattering functions are constant we find that:

$$P_{\text{est}}(\vec{k}) = P(\vec{k}) \quad (k_x = 0) \quad (38)$$

$$= (1 - f)^2 P(\vec{k}) \quad (k_x \neq 0) \quad (39)$$

If the Fourier modes \vec{k} are binned in spherical shells as a function of $k = |\vec{k}|$ then, as the value of k increases, the contribution of the mode with $k_x = 0$ becomes less important and $P_{\text{est}}(k) = (1 - f)^2 P(k)$ is an increasingly good approximation.

We now consider the case where a fraction f of redshifts are scattered by a fixed displacement along the x -axis, i.e. a convolution of the density field by a function U . Equation 26 is replaced by the relation

$$S(\vec{x}) = N_1 \sum_{x'} n(x', y, z) U(x - x') \quad (40)$$

with the Fourier transform

$$\tilde{S}(\vec{k}) = fN\tilde{U}(k_x) [\tilde{W}(\vec{k}) + \tilde{C}(\vec{k})] \quad (41)$$

Defining $\tilde{S}'(\vec{k}) = \tilde{S}(\vec{k}) - fN\tilde{U}(k_x)\tilde{W}(\vec{k})$ we find that

$$P_{\text{est}}(\vec{k})/P_c(\vec{k}) = (1 - f)^2 + 2f(1 - f) \text{Re}[\tilde{U}(k_x)] + f^2 |\tilde{U}(k_x)|^2 \quad (42)$$

For a simple shift $U(x) = \delta(x - x_0)$ we find that

$$P_{\text{est}}(\vec{k}) = [1 - 2f(1 - f)[1 - \cos(\vec{k}_x x_0)] P(\vec{k}) \quad (43)$$

These formulae are only approximations in the case of real data. Firstly, the sky is curved and the redshift scatters do not happen along a single axis of the cube. Secondly, the blunder fraction depends on redshift. Thirdly, the blunders due to line confusion are not a strict convolution of the density field, but a transformation in redshift $z_1 \rightarrow z_2$ of the form $z_2 = C(1 + z_1) - 1$, where C is a constant depending on the rest wavelengths of the lines. Fourthly, if a convolved redshift is shifted beyond the edge of the density cube, it does not “wrap around” as required by periodic boundary conditions. Fifthly, FKP estimation of the power spectrum is used rather than Equation 32.

In order to measure the distortion of our measured power spectrum due to redshift blunders for the real data, we therefore created Monte Carlo simulations of galaxy catalogues with a known input power spectrum and the same selection function $W(\vec{x})$ as each of our survey regions. We then applied the redshift blunder distributions of Figures 11 and 12 to the mock catalogues and re-measured the power spectrum. Comparison of the input and output power spectra, averaging over many Monte Carlo realizations, provided the correction factor due to redshift blunders. We tested our code by reproducing the relations given in Equations 37 and 42 in the flat-sky case.

Figure 13 plots the correction factors for the “angle-averaged” power spectrum $P(k)$ for each of the survey regions (taking a redshift interval $0.3 < z < 0.9$). We see that a good approximation for the correction for scales $k > 0.05 h \text{ Mpc}^{-1}$ is a constant, although a more significant correction is required for large scales $k < 0.05 h \text{ Mpc}^{-1}$. For $k > 0.05 h \text{ Mpc}^{-1}$ the approximately constant correction factor is not exactly equal to $(1 - f)^{-2}$ as predicted by Equation 39, where f is the average redshift blunder rate of the catalogue; this is due to the mis-estimation of the denominator of Equation 13 that occurs because $W(\vec{x})$ is determined from the galaxy redshift distribution including blunders, as described in Section 2.5. The Monte Carlo simulations performed here also correct for this small bias in power spectrum estimation.

3.3 Power spectrum measurement

In this study we analyzed a galaxy sample drawn from WiggleZ survey observations prior to July 2009 in SDSS regions of our optical imaging (9-hr, 11-hr, 15-hr). Figure 14 plots the (R.A., Dec.) distribution of these redshifts. We imposed the redshift cut $0.3 < z < 0.9$ in order to remove the tails of the redshift distribution which contain relatively few galaxies. A total of $N = 56,159$ galaxy redshifts remained. We then split the sample into three redshift slices $0.3 < z < 0.5$, $0.5 < z < 0.7$ and $0.7 < z < 0.9$.

We determined the effective redshift z_{eff} of our power spectrum estimate in each redshift slice by weighting each pixel in our 3D selection function by its contribution to the power spectrum error:

$$z_{\text{eff}}(k) = \sum_{\vec{x}} z \times \left(\frac{n_g(\vec{x})P(k)}{1 + n_g(\vec{x})P(k)} \right)^2 \quad (44)$$

where $n_g(\vec{x}) = (N_c N / V) W(\vec{x})$ is the galaxy number density

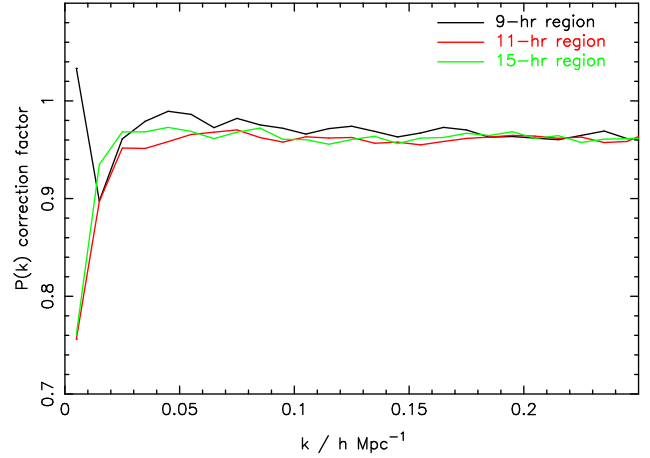


Figure 13. The power spectrum correction factor due to redshift blunders for each of the survey regions analyzed in this paper, for a redshift range $0.3 < z < 0.9$. The measured power spectrum must be divided by this factor in order to obtain an unbiased estimate of the true power spectrum.

in each grid cell and $P(k)$ is the power spectrum amplitude. In each case we used the best-fitting model power spectrum determined below. We evaluated this function at $k = 0.15 h \text{ Mpc}^{-1}$, although the dependence on scale is weak. The effective redshifts of each slice determined using equation 44 are $z_{\text{eff}} = (0.42, 0.59, 0.78)$.

We analyzed the three WiggleZ survey regions independently, resulting in a total of nine power spectrum measurements. We estimated the power spectrum up to a maximum Fourier wavenumber $k_{\text{max}} = 0.4 h \text{ Mpc}^{-1}$, assuming the value $P_0 = 2500 h^{-3} \text{ Mpc}^3$ for the weighting factor in Equation 9. This choice is motivated by our final measurement of the power spectrum amplitude presented below on scales $k \approx 0.15 h \text{ Mpc}^{-1}$, but does not have a strong influence on our results given that with the survey partially complete the measurements are limited by shot noise on most scales. Representative values for the other parameters in Section 3.1 are $(L_x, L_y, L_z) = (600, 600, 300) h^{-1} \text{ Mpc}$, $(n_x, n_y, n_z) = (256, 256, 128)$, $V = 0.1 h^{-3} \text{ Gpc}^3$ and $n_0 = 5 \times 10^{-5} h^3 \text{ Mpc}^{-3}$. We combined the Fourier amplitudes in angle-averaged bins of width $\Delta k = 0.01 h \text{ Mpc}^{-1}$.

The nine power spectrum measurements are plotted in Figure 15 together with a power spectrum model derived using a “standard” set of cosmological parameters together with a prescription for redshift-space distortions. The details of this model are described below in Section 4.1. The dashed and solid lines illustrate the input model, and the model convolved with the selection function for each region, respectively. The model provides an acceptable statistical fit to the measured power spectrum in each case.

The corresponding nine covariance matrices C_{ij} are plotted in Figure 16 as a correlation coefficient

$$r(i, j) = \frac{C_{ij}}{\sqrt{C_{ii} C_{jj}}} \quad (45)$$

Figure 16 demonstrates that the amplitude of the off-diagonal elements of the covariance matrices is small (note the choice of greyscale range).

We also measured power spectra in wavevector bins

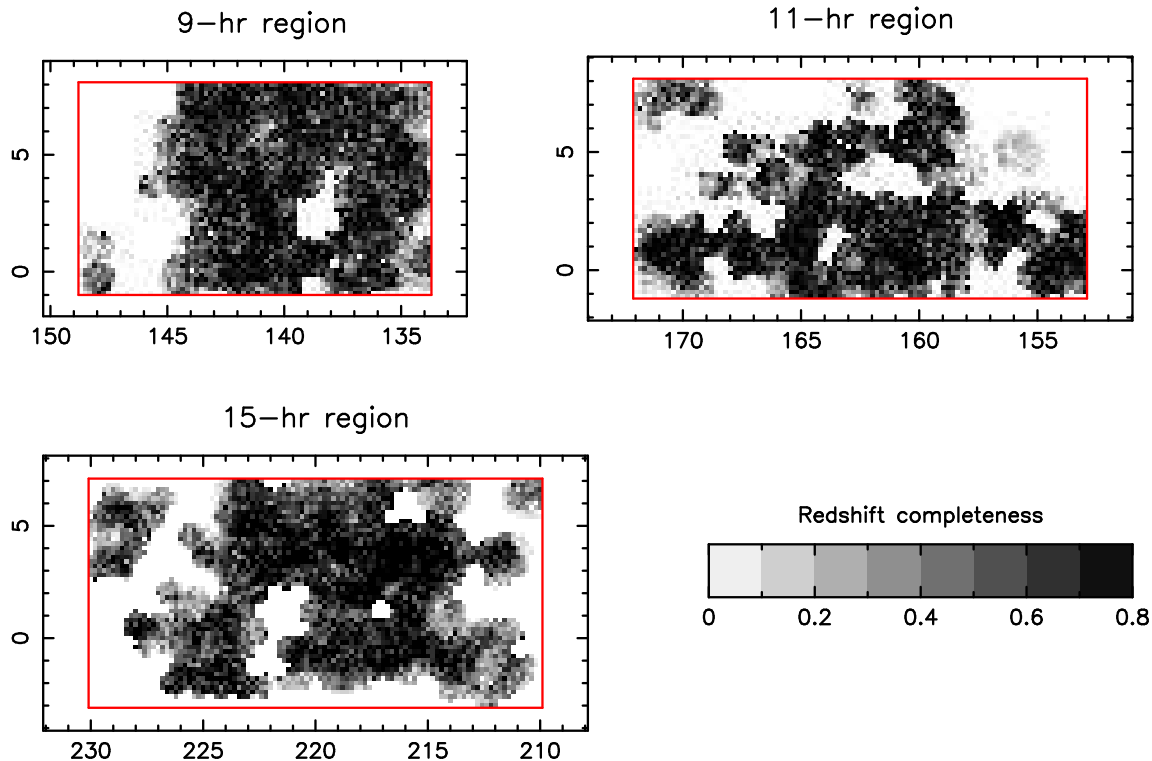


Figure 14. Greyscale map illustrating the completeness of the spectroscopic follow-up of the WiggleZ targets for the three survey regions analyzed in this paper. This Figure is generated by taking the ratio of the galaxy densities in the redshift and parent catalogues in small cells. The x -axis and y -axis of each panel are right ascension and declination, respectively.

($k_{\text{perp}}, k_{\text{par}}$) perpendicular and parallel to the line-of-sight, respectively (we now use Fourier bins of width $\Delta k = 0.02 h \text{ Mpc}^{-1}$ in each direction to increase the signal-to-noise ratio in each bin). This 2D power spectrum allows us to recover the redshift-space distortion parameters which produce an anisotropic galaxy power spectrum. Since in our analysis we orient the x -axis parallel to the line-of-sight to the centre of each survey region, we make the flat-sky approximation $k_{\text{perp}} = \sqrt{k_y^2 + k_z^2}$, $k_{\text{par}} = |k_x|$ in this analysis.

3.4 Systematic error study

We investigated the dependence of our power spectrum measurement on potential systematic errors in the survey selection function. In order to do this we re-constructed four different selection functions for the 9-hr region, analyzing the full redshift range $0.3 < z < 0.9$, with (extreme) variations in the method:

- We removed the variation of the completeness of the parent GALEX-SDSS sample with dust and GALEX exposure time described in Section 2.2, and instead assumed a constant density map.
- We removed the variation of redshift completeness across the field-of-view of the 2dF spectrograph described in Section 2.4, and instead assumed a constant redshift completeness.
- We removed the dependence of the survey redshift distribution on angular position described in Section 2.5, and instead used a position-independent radial selection function.

- We parameterized the redshift distribution for each magnitude slice using a 9th-order polynomial rather than a sum of two Gaussian functions.

In Figure 17 we plot the difference between the resulting power spectra measured for these four different selection functions and the fiducial power spectrum, in units of the standard deviation of the measurement at each scale. We note that these (extreme) variations in our understanding of the selection function typically cause up to $\approx 0.5\text{-}\sigma$ shifts in the power spectrum estimate. The exception is the parameterization of the redshift distribution, which causes large deviations in the very large-scale ($k < 0.03 h \text{ Mpc}^{-1}$) power spectrum. For the example being studied, we noted that the 9th-order polynomial fit was in fact providing a poorer match than the double Gaussian function to the observed redshift distributions, causing a spurious increase in measured large-scale power.

We conclude that our power spectrum measurements are likely to be robust against reasonable systematic variations in the selection function methodology. The selection function in Fourier space is compact and the corrections are only significant on the largest scales.

4 COSMOLOGICAL PARAMETER FITS

In this Section we present some initial comparisons between our power spectrum measurements and cosmological models. Our aim is to establish whether or not our measurements are consistent with the predictions of the standard ΛCDM

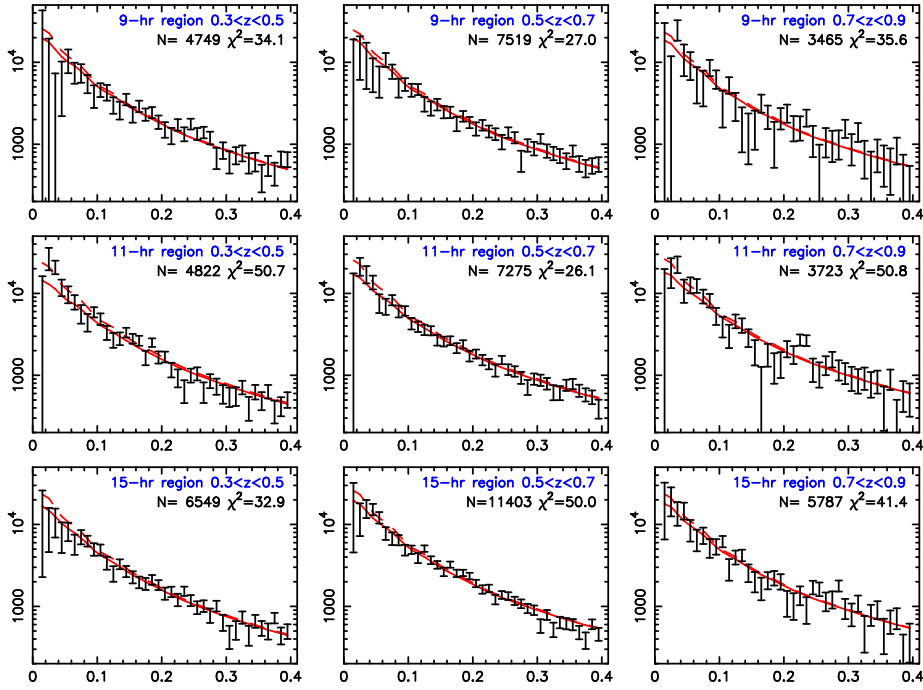


Figure 15. The 1D galaxy power spectrum for each of the survey regions and redshift slices analyzed in this paper. The data points in each plot are the power spectrum measured by FKP estimation. The dashed line is an (unconvolved) model power spectrum evaluated by integrating equation 46 over angles. We use cosmological parameters $\Omega_m = 0.3$, $\Omega_b/\Omega_m = 0.166$, $h = 0.72$, $n_s = 0.96$ and $\sigma_8 = 0.8$, together with values of the redshift-space distortion parameters and linear bias factor fit to the 2D power spectrum for each redshift slice. The solid line is the result of convolving this model power spectrum with the selection function for each region. The chi-squared statistic is calculated over the range $k < 0.4 h \text{ Mpc}^{-1}$ using the full covariance matrix. The x -axis and y -axis of each panel are Fourier wavenumber k in units of $h \text{ Mpc}^{-1}$ and power spectrum amplitude $P(k)$ in units of $h^{-3} \text{ Mpc}^3$, respectively.

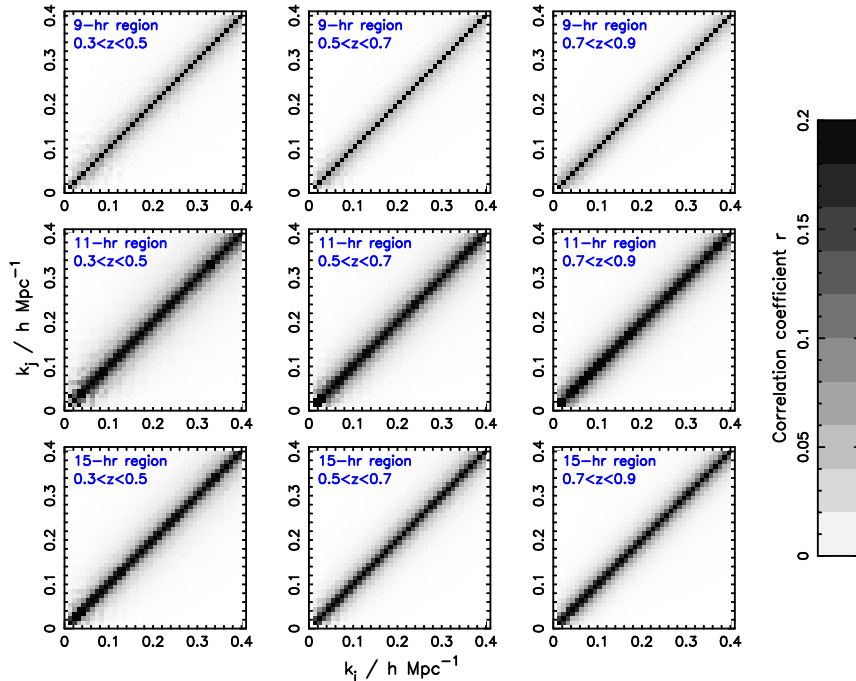


Figure 16. Greyscale plot of the correlation coefficient r of Equation 45 for each of the survey regions and redshift slices analyzed in this paper, indicating the degree of covariance between the power spectrum measurement in different Fourier bins. Note the choice of greyscale range such that the darkest shade corresponds to $r = 0.2$.

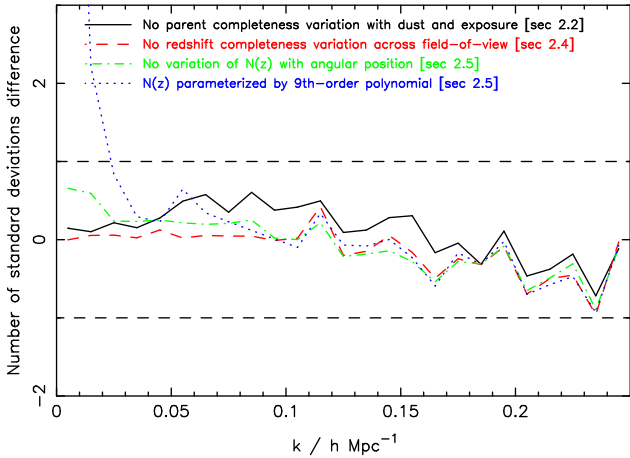


Figure 17. Variations in the power spectrum estimate for the 9-hr region, in units of standard deviations in the fiducial power spectrum, obtained by changes in the methodology used to construct the selection function.

framework with parameters determined by observations of the Cosmic Microwave Background radiation. Future papers will perform a more comprehensive analysis.

4.1 Model power spectra

We derived model matter power spectra $P_m(k)$ as a function of redshift using the CAMB software package (Lewis, Challinor & Lasenby 2000) which is based on CMBFAST (Seljak & Zaldarriaga 1996), including corrections for non-linear growth of structure using the fitting formulae of Smith et al. (2003) (`halofit=1` in CAMB). Throughout this analysis (unless otherwise noted) we fix values for the Hubble parameter $h = 0.72$, scalar index of spectral fluctuations $n_s = 0.96$ and normalization $\sigma_8 = 0.8$, and vary only the matter density Ω_m and the baryon fraction Ω_b/Ω_m . Our choices of parameter values are consistent with recent observations of the Cosmic Microwave Background radiation (Komatsu et al. 2009).

For this initial parameter fitting we assumed a linear bias factor b for the galaxy population. The assumption of linear bias will be investigated in more detail in future studies through the use of mock catalogues generated from dark matter simulations, analysis of the galaxy bispectrum (e.g. Verde et al. 2002; Nishimichi et al. 2007), and measurements of the halo occupation distribution of WiggleZ galaxies (e.g. Zehavi et al. 2005; Blake, Collister & Lahav 2008). We note that in the current analysis the value of the bias factor is significantly degenerate with the choice of σ_8 (such that $b \propto 1/\sigma_8$).

We modified this real-space matter power spectrum to include redshift-space distortions, which we characterized in the standard manner using two parameters. The first parameter, f , models the effect of large-scale coherent infall velocities. In linear theory for the growth of fluctuations, f is related to the linear growth factor $D(a)$ at scale factor a by $f = d \ln D / d \ln a$. This functional form is well-approximated by $f = \Omega_m(z)^\gamma$ where $\Omega_m(z)$ is the matter density measured by an observer at redshift z , and $\gamma \approx 0.55$ for a standard Λ CDM cosmology. Coherent velocities can also be parameterized by $\beta = f/b$, introducing a dependence on galaxy

type via the bias factor. The second parameter, σ_v (in units of $h \text{ km s}^{-1}$), describes small-scale random virialized velocities, for which we assumed an exponential pairwise distribution. The overall effect on the galaxy power spectrum P_{gal} is to induce an anisotropic distortion dependent on the angle θ of the wavevector to the line-of-sight, parameterized by $\mu = \cos \theta$:

$$P_{\text{gal}}(k, \mu) = b^2 P_m(k) \frac{(1 + f\mu^2/b)^2}{1 + (k H_0 \sigma_v \mu)^2} \quad (46)$$

4.2 Fits to the 2D power spectra in redshift slices

We fitted these models to the nine independent 2D power spectra split into tangential and radial components, in order to determine the redshift-space distortion parameters and test the Λ CDM self-consistency relation $\beta \approx \Omega_m(z)^{0.55}/b$ as a function of redshift. In this initial analysis we fixed the matter density parameter $\Omega_m = 0.3$ and baryon fraction $\Omega_b/\Omega_m = 0.166$ (similar to the parameters listed in Komatsu et al. (2009) that provide the best fit to the 5-year data set of the Wilkinson Microwave Anisotropy Probe (WMAP); we fix $\Omega_m = 0.3$ to match the value assumed for the distance-redshift relation in our power spectrum analysis). We then varied the redshift-space parameters f and σ_v and the bias factor b , convolving each model power spectrum with the survey selection function for each region and minimizing the chi-squared statistic calculated using the full covariance matrices. For each redshift slice we combined the results from the three survey regions. The best-fitting models produce a good fit to the measured power spectrum, as evidenced by the values of the chi-squared statistic in the three redshift slices: $\chi^2 = (1113.9, 1229.6, 1069.2)$ for 1137 degrees of freedom.

The measurements of the growth rates at each effective redshift $z_{\text{eff}} = (0.42, 0.59, 0.78)$ are $f = (0.73 \pm 0.09, 0.75 \pm 0.09, 0.71 \pm 0.14)$, marginalizing over the parameters σ_v and b , where 1- σ error ranges are indicated. These should be compared to the Λ CDM prediction for $\Omega_m(0) = 0.3$: $f = (0.72, 0.78, 0.83)$. We find that the model successfully passes this test of self-consistency. Our measurements of the growth rate are compared with the model in Figure 18 by plotting the quantity $f \times \sigma_{8,\text{mass}}(z)$ versus redshift. Previously-published results are also indicated, as summarized by Song & Percival (2009). The WiggleZ Survey data provides a growth measurement across the redshift range $0.4 < z < 0.8$ with a precision similar to previous work at $z < 0.4$. We highlight in particular the 20% accuracy of our measurement at $z = 0.78$. A future study will perform a more detailed analysis of these results.

The fitted values of the pairwise velocity dispersion in each redshift slice are $\sigma_v = (354 \pm 41, 294 \pm 31, 216 \pm 58) h \text{ km s}^{-1}$ (marginalizing over f and b). We find evidence that the pairwise small-scale velocity dispersion of WiggleZ galaxies systematically decreases with increasing redshift. The measured bias factors for each redshift slice are $b = (0.93 \pm 0.03, 1.08 \pm 0.03, 1.20 \pm 0.06)$ (marginalizing over f and σ_v). We can compare these galaxy bias measurements to those deduced from the WiggleZ survey small-scale correlation function measurements: for three redshift slices similar to those analyzed here, Blake et al. (2009) obtained $b = (1.01, 1.27, 1.27)$ (although assuming a higher

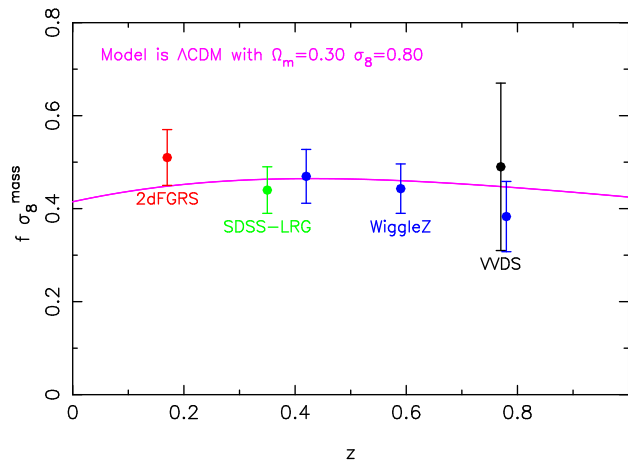


Figure 18. Measurements of the growth rate of structure, f , obtained in three redshift slices by fitting WiggleZ survey data in three survey regions. The values of f are weighted by $\sigma_{8,\text{mass}}(z)$ as discussed by Song & Percival (2009). The measurements are compared to results previously published for the 2dFGRS, SDSS LRG, and VIRMOS-VLT Deep Survey (VVDS) samples, as collected by Song & Percival. A prediction for the Λ CDM cosmological model with $\Omega_m = 0.3$ and $\sigma_8 = 0.8$ is overlotted.

value of $\sigma_8 = 0.9$). The main cause of this difference is the superior determination of β in the current analysis. Other issues with this comparison include: (i) galaxy bias is a scale-dependent function, (ii) small-scale pairwise velocities were not been modelled in the Blake et al. (2009) analysis, (iii) the power-law correlation function model assumed in Blake et al. (2009) breaks down at large scales.

4.3 Stacked 1D power spectra

Using these model fits we can combine the nine 1D power spectrum measurements in the different regions and redshift slices into a single “stacked” survey 1D power spectrum using inverse-variance weighting. The difficulty with this step is that the power spectrum amplitude in each region is modulated by a different level of convolution with the selection function, as illustrated by Figure 15. In addition, the shape of the power spectrum varies with redshift in accordance with the differing redshift-space distortion parameters and galaxy bias factors.

Therefore, before combining the results in the different regions and redshift slices, we performed an approximate “de-convolution” of amplitude by multiplying the power spectra by a correction factor equal to the scale-dependent ratio of the convolved and unconvolved model power spectra, i.e. the ratio of the solid and dashed curves plotted in Figure 15. (In detail we did not use the model power spectra to generate these corrections but a “reference” power spectrum in which the baryon oscillation features have been smoothed out, i.e. the “no-wiggles” power spectrum of Eisenstein & Hu (1998). We preferred to correct the amplitude using a wiggle-free power spectrum to avoid spuriously introducing apparent baryon oscillations into the combined power spectrum). We additionally corrected the measurement in each Fourier bin by the angle-averaged ratio of the redshift-space galaxy power spectrum (using the best-fitting values of β and σ_v for

each redshift slice) to the real-space matter power spectrum at redshift $z = 0.6$. Following these corrections, the nine power spectra “line up” with consistent shape and amplitude, and can be combined. In Figure 19 we show separate combinations of power spectra across survey regions in each redshift slice, and across redshift slices in each survey region. The combination of all nine power spectra is presented in Figure 20; the lower panel indicates the fractional accuracy of the measurement, which approaches 5% in Fourier bins of width $\Delta k = 0.01 h \text{ Mpc}^{-1}$. The scale dependence of the fractional accuracy is determined by a balance between the increasing number of Fourier modes contributing to each successive bin (tending to decrease the error), and the increasing importance with k of shot noise relative to cosmic variance (tending to increase the error). Finally, in Figure 21 we display the 2D power spectra for each redshift slice, combining different regions in the manner described above.

4.4 Fits for matter and baryon densities

As a final exercise we fitted the measured power spectra for the cosmological matter and baryon densities (parameterized by Ω_m and $f_b = \Omega_b/\Omega_m$). We tried three different initial approaches to this analysis, with increasing degrees of sophistication:

- First, we generated unconvolved, real-space, non-linear power spectra and fitted the combined survey data points plotted in the upper panel of Figure 20 by varying Ω_m , f_b and the bias factor b .
- Second, we fitted the convolved, redshift-space 1D power spectra in each of the survey regions and redshift slices, fixing the redshift-space distortion parameters β and σ_v at the best-fitting measurements using the 2D power spectrum fits at each redshift and varying Ω_m , f_b and b .
- Third, we fitted the convolved, redshift-space 2D power spectra, fixing the value of σ_v at the best-fitting values. We varied Ω_m , f_b and the bias factor b , determining the value $\beta = \Omega_m(z)^{0.55}/b$ in each case (assuming the Λ CDM model). For each different value of Ω_m , we scaled σ_8 assuming the “WMAP normalization” (Komatsu 2009, Section 5.5) and also scaled the geometry of the survey box in accordance with each trial cosmology: given a fiducial co-moving distance D_{fid} and Hubble parameter H_{fid} for a redshift slice calculated using $\Omega_m = 0.3$, and also given trial values D , H corresponding to a different value of Ω_m , the width of Fourier bins tangential and radial to the line-of-sight scales as D/D_{fid} and H_{fid}/H , respectively; furthermore the volume of the box (hence amplitude of the measured power spectrum) scales as $(D/D_{\text{fid}})^2 \times (H_{\text{fid}}/H)$.

Figure 22 displays the probability contours in the 2D space of Ω_m and $f_b = \Omega_b/\Omega_m$, marginalizing over the bias factor, for each of the three approaches described above. The different methods produce broadly consistent results, and the best-fitting values are in good agreement with those determined from the latest measurements of the temperature fluctuations of the Cosmic Microwave Background radiation (Komatsu et al. 2009).

The probability contours in Figure 22 display evidence of the well-known degeneracy between Ω_m and Ω_b/Ω_m in the determination of the overall shape of the matter power spectrum, which is exacerbated by the fact that we cannot

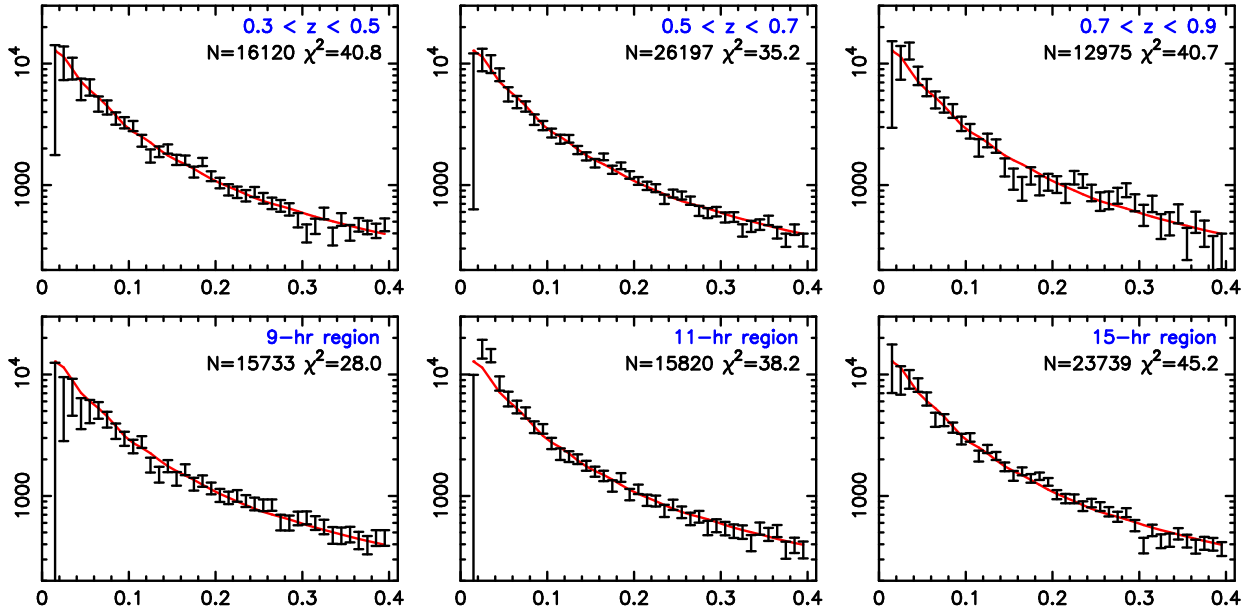


Figure 19. The power spectra determined by combining the measurements in the different survey regions (for each redshift slice) and different redshift slices (for each survey region). Before combination, we adjust the shapes of the power spectra to allow for the differing degrees of convolution with the selection function and the differing redshift-space effects. The solid line in the panel has been generated by combining the best-fitting model power spectra in a similar manner. The x -axis and y -axis of each panel are Fourier wavenumber k in units of $h \text{ Mpc}^{-1}$ and power spectrum amplitude $P(k)$ in units of $h^{-3} \text{ Mpc}^3$, respectively.

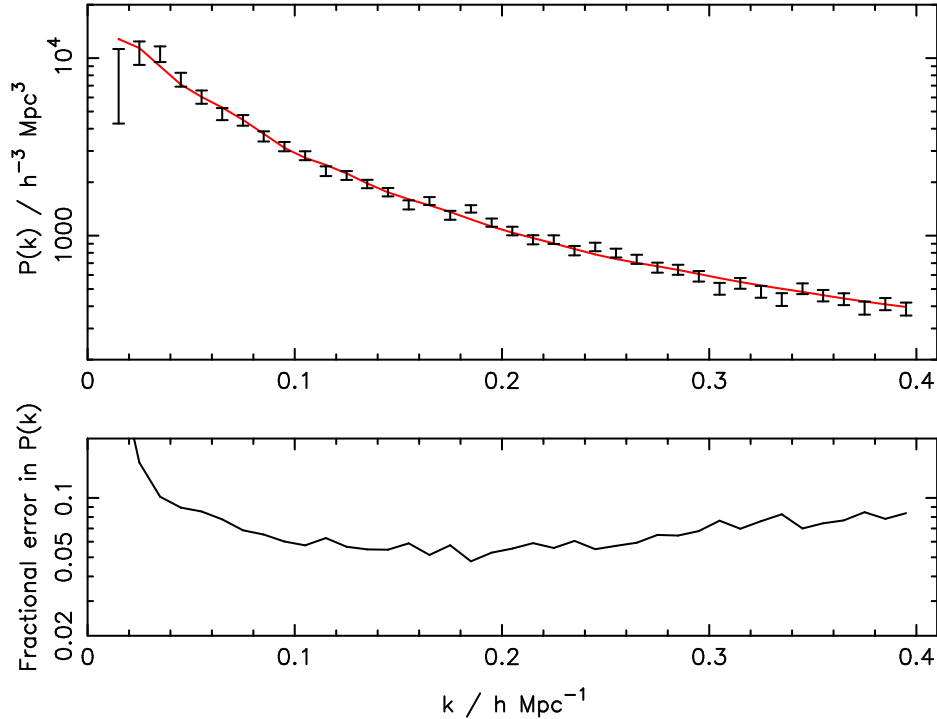


Figure 20. *Upper panel:* The power spectrum determined by combining the measurements in the different survey regions and redshift slices analyzed in this paper using inverse-variance weighting. Before combination, we adjust the shapes of the power spectra to allow for the differing degrees of convolution with the selection function and the differing redshift-space effects. The solid line in the panel has been generated by combining the best-fitting model power spectra in a similar manner. *Lower panel:* The fractional error in the combined power spectrum as a function of Fourier wavenumber k .

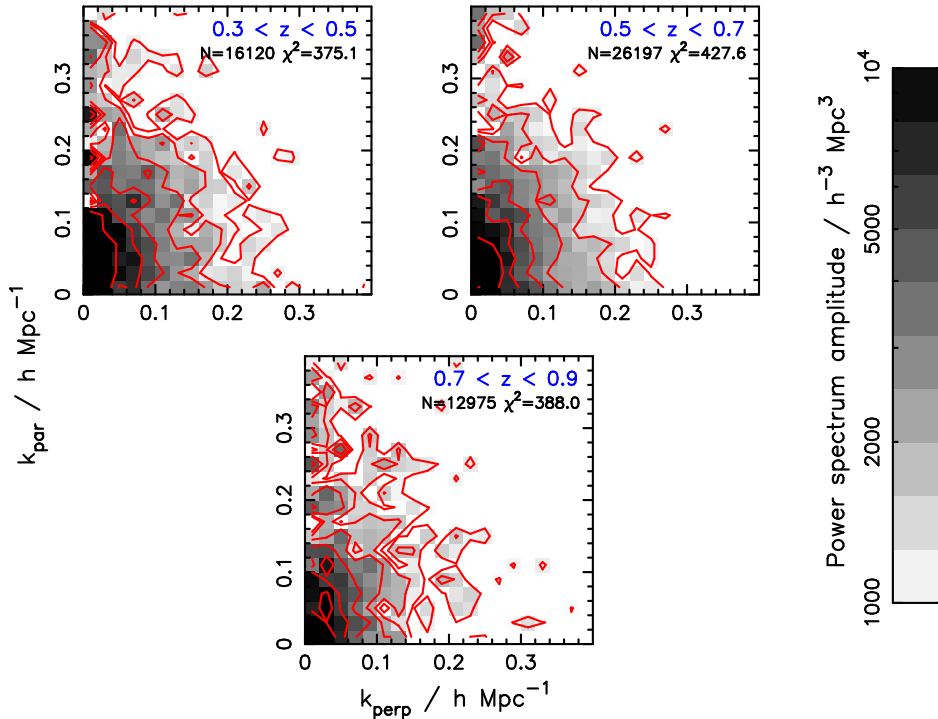


Figure 21. The 2D galaxy power spectra for each of the redshift slices analyzed in this paper, obtained by combining measurements in different survey regions, and plotted as a function of wavevectors ($k_{\text{perp}}, k_{\text{par}}$) tangential and radial to the line-of-sight, respectively. The function is represented using both greyscale and contours; the contour levels are logarithmically spaced between $P = 1000$ and $10,000 h^{-3} \text{ Mpc}^3$. The non-circularity of the contours encodes the imprint of large-scale galaxy peculiar velocities, as discussed in the text.

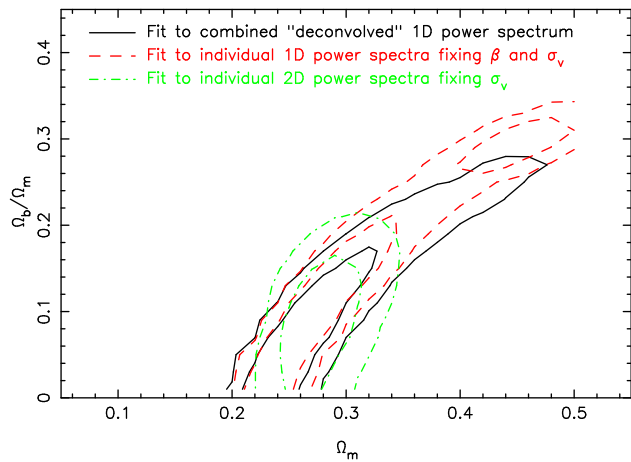


Figure 22. Probability contours of Ω_m and Ω_b/Ω_m fitting to WiggleZ survey power spectra using the three different approaches described in the text. The inner and outer contours for each set enclose 68% and 95% of the likelihood, respectively.

yet detect the imprint of the baryon acoustic oscillations in our power spectrum measurement. This degeneracy will be broken as the WiggleZ Survey progresses.

5 CONCLUSIONS

In this paper we have described our method of determining the selection function of the WiggleZ Dark Energy Survey, and have presented the current measurement of the large-scale galaxy power spectrum using 56,159 redshifts of bright emission-line galaxies spanning redshifts $0.3 < z < 0.9$. This sample constitutes approximately 25% of the final WiggleZ survey. We have quantified and categorized the redshift blunder rate and determined its effect on the power spectrum measurement via analytical calculations and detailed simulations. We conclude that:

- The selection function of the WiggleZ survey is complicated by the proximity of the faint magnitude threshold to the completeness limit of the input catalogues, in particular for the GALEX UV data. We quantified the incompleteness in the parent target catalogue as a function of GALEX exposure time and Galactic extinction via fitting formulae.
- We adopted a Monte Carlo technique to determine the relative completeness of the spectroscopic follow-up at any position. This technique allows for the complex overlapping of survey pointings and for the systematic variation of redshift completeness across the 2-degree field-of-view of the instrument. We also allowed for the magnitude prioritization of the spectroscopic follow-up which results in a position-dependent galaxy redshift distribution.
- The WiggleZ survey contains redshift blunders resulting from emission-line confusion (most significantly, [OIII], H β and H α mis-identified as [OII]) and from sky emission lines mis-identified as [OII]. The overall blunder rate is about 5%.

The effect of the redshift blunders on the power spectrum measurement is well-approximated as a constant reduction in amplitude for scales $k > 0.05 h \text{ Mpc}^{-1}$ combined with an enhanced level of reduction for large scales $k < 0.05 h \text{ Mpc}^{-1}$.

- We measured 1D (angle-averaged) and 2D (binned in tangential and radial modes) galaxy power spectra for nine independent survey regions and redshift slices using the method of Feldman, Kaiser & Peacock (1994). The 1D power spectrum for the whole sample, combining these measurements, has a fractional accuracy of about 5% in Fourier bins of width $\Delta k = 0.01 h \text{ Mpc}^{-1}$. The 2D power spectra show the expected anisotropic signatures of redshift-space distortions due to large-scale coherent infall and small-scale virialized motions.

- The power spectrum data are well-described by a model power spectrum with matter and baryon densities consistent with those determined from observations of the Cosmic Microwave Background radiation. The model includes non-linear corrections, redshift-space distortions and a linear galaxy bias factor.

- The 2D power spectra allow us to measure the growth rate of structure across the redshift range $0.4 < z < 0.8$. We obtain results similar in precision to previous determinations at $z < 0.4$, including a measurement at $z = 0.78$ with 20% accuracy.

Future studies will present full cosmological parameter fits and combinations of these results with other datasets, including implications for the growth of cosmic structure and Gaussianity of the initial conditions, and extend these analyses to the final WiggleZ survey catalogues.

ACKNOWLEDGMENTS

We thank an anonymous referee for useful comments on the submitted version of this paper.

We acknowledge financial support from the Australian Research Council through Discovery Project grants funding the positions of SB, MP, GP and TD. SMC acknowledges the support of the Australian Research Council through a QEII Fellowship. MJD thanks the Gregg Thompson Dark Energy Travel Fund for financial support.

GALEX (the Galaxy Evolution Explorer) is a NASA Small Explorer, launched in April 2003. We gratefully acknowledge NASA's support for construction, operation and science analysis for the GALEX mission, developed in co-operation with the Centre National d'Etudes Spatiales of France and the Korean Ministry of Science and Technology.

Finally, the WiggleZ survey would not be possible without the dedicated work of the staff of the Anglo-Australian Observatory in the development and support of the AAOmega spectrograph, and the running of the AAT.

REFERENCES

Bardeen J.M., Bond J.R., Kaiser N., Szalay A.S., 1986, *ApJ*, 304, 15
 Blake C.A., Glazebrook K., 2003, *ApJ*, 594, 665
 Blake C.A., Bridle S.L., 2005, *MNRAS*, 363, 1329

Blake C.A., Collister A., Bridle S., Lahav O., 2007, *MNRAS*, 374, 1527
 Blake C.A., Collister A., Lahav O., 2008, *MNRAS*, 385, 1257
 Blake C.A. et al., 2009, *MNRAS*, 395, 240
 Bond J.R., Efstathiou G., 1984, *ApJ*, 285, 45
 Carroll S.M., Press W.H., Turner E.L., 1992, *ARA&A*, 30, 499
 Cole S. et al., 2005, *MNRAS*, 362, 505
 Colless M. et al., 2001, *MNRAS*, 328, 1039
 Conway E., 2005, *MNRAS*, 356, 456
 Cresswell J.G., Percival W.J., 2009, 392, 682
 Croft R., Weinberg D.H., Bolte M., Burles S., Hernquist L., Katz N., Kirkman D., Tytler D., 2002, *ApJ*, 581, 20
 Dekel A., Lahav O., 1999, *ApJ*, 520, 24
 Drinkwater M. et al., 2010, *MNRAS*, 401, 1429
 Eisenstein D.J. et al., 2001, *AJ*, 122, 2267
 Eisenstein D.J., Hu W., 1998, *ApJ*, 518, 2
 Eisenstein D.J. et al., 2005, *ApJ*, 633, 560
 Elgaroy O. et al., 2002, *PhRvL*, 89, 1301
 Feldman H.A., Kaiser N., Peacock J.A., 1994, *ApJ*, 426, 23
 Fry J.N., Scherrer R.J., 1994, *ApJ*, 429, 36
 Glazebrook K., Blake C.A., 2005, *ApJ*, 631, 1
 Gott J.R., Dickinson M., Melott A.L., 1986, *ApJ*, 306, 341
 Hamilton A.J.S., 1992, *ApJ*, 385, 5
 Hamilton A.J.S., 2001, *MNRAS*, 322, 419
 Hawkins E. et al., 2003, *MNRAS*, 346, 78
 Heath D.J., 1977, *MNRAS*, 179, 351
 Holtzman J.A., 1989, *ApJS*, 71, 1
 Guzzo L. et al., 2008, *Nature*, 451, 541
 Hoyle F., Outram P.J., Shanks T., Croom S.M., Boyle B.J., Loaring N.S., Miller L., Smith R.J., 2002, *MNRAS*, 329, 336
 Hu W., Sugiyama N., 1996, *ApJ*, 471, 542
 Hu W., Haiman Z., 2003, *Phys. Rev. D*, 68, 063004
 Huetsi G., 2006, *A&A*, 459, 375
 James J.B., Lewis G.F., Colless M., 2007, *MNRAS*, 375, 128
 Jing Y., 2005, *ApJ*, 620, 559
 Jeong D., Komatsu E., 2006, *ApJ*, 651, 619
 Komatsu E. et al., 2009, *ApJS*, 180, 330
 Lewis A., Challinor A., Lasenby A., 2000, *ApJ*, 538, 473
 Linder E.V., Jenkins A., 2003, *MNRAS*, 346, 573
 McDonald P. et al., 2005, *ApJ*, 635, 761
 McDonald P. et al., 2006, *ApJS*, 163, 80
 McDonald P., 2007, *PhRvD*, 75, 3514
 Morrissey P. et al., 2007, *ApJS*, 173, 682
 Nishimichi T., Kayo I., Hikage C., Yahata K., Taruya A., Jing Y.P., Sheth R.K., Suto Y., 2007, *PASJ*, 59, 93
 Outram P.J., Hoyle F., Shanks T., Croom S.M., Boyle B.J., Miller L., Smith R.J., Myers A.D., 2003, *MNRAS*, 342, 483
 Padmanabhan N. et al., 2007, *MNRAS*, 378, 852
 Peacock J.A., Dodds S.J., 1994, *MNRAS*, 267, 1020
 Percival W. et al., 2001, *MNRAS*, 327, 1313
 Percival W. et al., 2002, *MNRAS*, 337, 1068
 Percival W. 2005, *A&A*, 443, 819
 Percival W. et al., 2007a, *ApJ*, 657, 645
 Percival W. et al., 2007b, *MNRAS*, 381, 1053
 Percival W., White M., 2009, *MNRAS*, 393, 297
 Pope A. et al., 2004, *ApJ*, 607, 655
 Ross N. et al., 2009, *ApJ*, 697, 1634
 Sanchez A., Cole S., 2008, *MNRAS*, 385, 830
 Scherrer R.J., Weinberg D.H., 1998, *ApJ*, 504, 607
 Sefusatti E., Komatsu E., 2007, *PhRvD*, 76, 3004
 Seljak U. et al., 2005, *PhRvD*, 71, 3515
 Seljak U., Zaldarriaga M., 1996, *ApJ*, 469, 437
 Seo H.-J., Eisenstein D.J., 2003, *ApJ*, 598, 720
 Smith R.E. et al., 2003, *MNRAS*, 341, 1311
 Smith R.E., Scoccimarro R., Sheth R.K., 2007, *PhRvD*, 75, 3512
 Song Y.-S., Percival W.J., 2009, *JCAP*, 10, 4
 Tadros H., Efstathiou G., 1996, *MNRAS*, 282, 1381
 Tegmark M., 1997, *PhRvL*, 79, 3806

- Tegmark M., Bromley B.C., 1999, ApJ, 518, 69
Tegmark M. et al., 2004a, ApJ, 606, 702
Tegmark M. et al., 2004b, PhRvD, 69, 3501
Tegmark M. et al., 2006, PhRvD, 74, 3507
Verde L. et al., 2002, MNRAS, 335, 432
Wang Y., 2008, JCAP, 05, 021
White M., Song Y.-S., Percival W.J., 2009, MNRAS, 397, 1348
Wild V. et al., 2005, MNRAS, 356, 247
Xu K. et al., 2005, ApJ, 619, 11
York D.G. et al., 2000, AJ, 120, 1579
Zehavi I. et al., 2005, ApJ, 630, 1